

Ductile damage model for metal forming simulations including refined description of void nucleation

A. V. Shutov^{a,b,*}, C. B. Silbermann^c, J. Ihlemann^c

^a*Laurentyev Institute of Hydrodynamics, Department of Solid Mechanics, Pr. Laverentyeva 15, 630090 Novosibirsk, Russia*

^b*Novosibirsk State University, Pirogova 2, 630090 Novosibirsk, Russia*

^c*Technische Universität Chemnitz, Department of Solid Mechanics, Reichenhainer Strasse 90, 09126 Chemnitz, Germany*

Abstract

We address the prediction of ductile damage and material anisotropy accumulated during plastic deformation of metals. A new model of phenomenological metal plasticity is proposed which is suitable for applications involving large deformations of workpiece material. The model takes combined nonlinear isotropic/kinematic hardening, strain-driven damage and rate-dependence of the stress response into account. Within this model, the work hardening and the damage evolution are fully coupled. The description of the kinematics is based on the double multiplicative decomposition of the deformation gradient proposed by Lion. An additional multiplicative decomposition is introduced in order to account for the damage-induced volume increase of the material. The model is formulated in a thermodynamically admissible manner. Within a simple example of the proposed framework, the material porosity is adopted as a rough measure of damage.

A new simple void nucleation rule is formulated based on the consideration of various nucleation mechanisms. In particular, this rule is suitable for materials which exhibit a higher void nucleation rate under torsion than in case of tension.

The material model is implemented into the FEM code Abaqus and a simulation of a deep drawing process is presented. The robustness of the algorithm and the performance of the formulation is demonstrated.

Keywords:

B. anisotropic material; B. cyclic loading; B. elastic-viscoplastic material; B. finite strain; ductile damage

2000 MSC: 74R20, 74C20

*Corresponding author. Tel.: +7 383 333 17 46; fax: +7 383 333 16 12.
Email address: alexey.v.shutov@gmail.com (A. V. Shutov)

Nomenclature

$\mathbf{1}$	identity tensor
$\mathbf{F}, \mathbf{F}_{\text{ep}}^{\text{por}}$	deformation gradient and its elasto-plastic part (cf. (1))
$\mathbf{F}_i, \mathbf{F}_{ii}^{\text{por}}$	dissipative parts of deformation (cf. (3), (4))
$\hat{\mathbf{F}}_e, \check{\mathbf{F}}_{ie}$	conservative parts of deformation (cf. (3), (4))
$\mathbf{C}, \mathbf{C}_{\text{ep}}^{\text{por}}$	total and elasto-plastic right Cauchy-Green tensors (cf. (7) ₁)
$\mathbf{C}_i, \mathbf{C}_{ii}^{\text{por}}$	(dissipative) tensors of right Cauchy-Green type (cf. (7) ₂ , (8) ₁)
$\hat{\mathbf{C}}_e, \check{\mathbf{C}}_{ie}$	(conservative) tensors of right Cauchy-Green type (cf. (7) ₃ , (8) ₂)
\mathbf{L}	velocity gradient tensor
$\hat{\mathbf{L}}_i$	inelastic velocity gradient (cf. (10) ₁)
$\check{\mathbf{L}}_{ii}$	inelastic velocity gradient of substructure (cf. (11) ₁)
\mathbf{D}	strain rate tensor (stretching tensor)
$\hat{\mathbf{D}}_i$	inelastic strain rate (cf. (10) ₂)
$\check{\mathbf{D}}_{ii}$	inelastic strain rate of substructure (cf. (11) ₂)
s, s_d, s_e	inelastic arc-length and its parts (cf. (12))
$\mathbf{T}, \tilde{\mathbf{T}}$	Cauchy stress and 2nd Piola-Kirchhoff stress
$\mathbf{S}, \mathbf{S}_{\text{ep}}^{\text{por}}$	Kirchhoff stress and Kirchhoff-like stress (cf. (13))
$\hat{\mathbf{S}}_{\text{ep}}, \mathbf{T}_{\text{ep}}^{\text{por}}$	pull-backs of \mathbf{S}_{ep} to $\hat{\mathcal{K}}$ and $\check{\mathcal{K}}$ (cf. (14), (16))
$\hat{\mathbf{X}}, \mathbf{X}, \check{\mathbf{X}}$	backstresses on $\hat{\mathcal{K}}, \check{\mathcal{K}}, \check{\mathcal{K}}$ (cf. (18), (19), (28) ₂)
$\hat{\Sigma}, \check{\Sigma}$	effective stress on $\hat{\mathcal{K}}$ and Mandel-like backstress on $\check{\mathcal{K}}$ (cf. (21), (20))
R	isotropic hardening (stress) (cf. (28) ₃ , (42))
f	yield function (rate-dependent overstress) (cf. (42))
\mathbf{A}^{D}	deviatoric part of a second-rank tensor
$\overline{\mathbf{A}}$	unimodular part of a second-rank tensor (cf. (25))
\mathbf{A}^{T}	transposition of a second-rank tensor
$\text{sym}(\mathbf{A})$	symmetric part of a second-rank tensor
$\ \mathbf{A}\ $	Frobenius norm of a second-rank tensor
$\mathbf{A} : \mathbf{B}$	scalar product of two second-rank tensors
$\rho_{\text{R}}, \rho_{\text{por}}$	mass densities in $\check{\mathcal{K}}$ and $\check{\mathcal{K}}^{\text{por}}$
Φ	damage-induced volume change (cf. (2))
N	void number per unit volume in $\check{\mathcal{K}}$

1. Introduction

Dealing with metal forming applications, it is often necessary to assess the mechanical properties of the resulting engineering components, including the remaining bearing capacity, accumulated defects, and residual stresses. Thus, a state-of-the-art model for metal forming simulations should account for various nonlinear phenomena. If the residual stresses and the spring back are of particular interest, such a model should include the combined isotropic/kinematic hardening. For

some metals, however, the influence of ductile damage induced by plastic deformation should be taken into account as well. In spite of widespread applications involving large plastic deformations accompanied by kinematic hardening and damage, only few material models cover these effects (cf. Simo and Ju (1989); Menzel et al. (2005); Lin and Brocks (2006); Grammenoudis et al. (2009); Bammann and Solanki (2010); Bröcker and Matzenmiller (2014)).

In the current study we advocate the approach to plasticity/viscoplasticity based on the multiplicative decomposition of the deformation gradient. This approach is gaining popularity due to its numerous advantages like the absence of spurious shear oscillations, the absence of non-physical dissipation in the elastic range and the weak invariance under the change of the reference configuration (Shutov and Ihlemann, 2014). The main purpose of the current publication is to promote the phenomenological damage modeling within the multiplicative framework. Toward that end, the model of finite strain viscoplasticity proposed by Shutov and Kreißig (2008a) is extended to account for ductile damage. The original viscoplastic model takes the isotropic hardening of Voce type and the kinematic hardening of Armstrong-Frederick type into account. The model is based on a double multiplicative split of the deformation gradient, considered by Lion (2000).¹ Both the original model and its extension are thermodynamically consistent. We aim at the simplest possible extension which takes the following effects into account:

- nonlinear kinematic and isotropic hardening;
- inelastic volume change due to damage-induced porosity;
- damage-induced deterioration of elastic and hardening properties.

In this vein, we assume that the elastic properties deteriorate with increasing damage and remain isotropic at any stage of deformation. The assumption of elastic isotropy is needed to exclude the plastic spin from the flow rule, thus reducing the flow rule to six dimensions.

The interaction between damage and strain hardening is explicitly captured by the extended model. It is known that the mechanisms of the isotropic and kinematic hardening are not identical (cf. Barlat et al. (2003)). Therefore, the isotropic and kinematic contributions to the overall hardening deteriorate differently with increasing damage. Concerning the coupling in the opposite direction, the accumulated plastic anisotropy has a clear impact on the rate of damage accumulation upon the strain path change.

Since the proposed model is a generalization of the existing viscoplasticity model, some well-established numerical procedures can be used. The model is formulated as an open framework, suitable for further extension. Physically motivated relations describing void nucleation, growth, and coalescence can be implemented in a straightforward way, thus enriching the constitutive formulation. The restrictions imposed on these relations by the second law of thermodynamics are obtained in an explicit form.

¹ The seminal idea of the double split was already used by several authors to capture the nonlinear kinematic hardening (Helm, 2001; Tsakmakis and Willuweit, 2004; Dettmer and Reese, 2004; Hartmann et al., 2008; Henann and Anand, 2009; Brepols et al., 2013; Zhu et al., 2013; Brepols et al., 2014). It was also implicitly adopted by Menzel et al. (2005); Johansson et al. (2005). A simple extension to distortional hardening was presented by Shutov et al. (2011).

A new refined void nucleation rule is introduced in this paper for porous ductile metals with second phases. This evolution law contains dependencies on the eigenvalues of the (effective) stress. The rule is based on consideration of various nucleation mechanisms, like debonding of second phase particles under tensile and shear loading or crushing of the particles under high hydrostatic stress. Therefore, the material parameters possess a clear mechanical interpretation, which simplifies the parameter identification on the basis of microstructural observations or molecular dynamics simulations.

The material model is validated using the experimental flow curves presented by Horstemeyer (1998) for a cast A356 aluminium alloy as well as some experimental data on void nucleation published by Horstemeyer et al. (2000).

We close this introduction with a few remarks regarding notation. The entire presentation is coordinate free (cf. Shutov and Kreißig (2008b)). Therefore, upright subscripts in the notation do not indicate tensorial index but stand for different deformation mechanisms such as “e” for *elastic* and “i” for *inelastic*. Throughout this article, bold-faced symbols denote first- and second-rank tensors in \mathbb{R}^3 . Symbol $\mathbf{1}$ stands for the identity tensor. The deviatoric part of a tensor is given by $\mathbf{A}^D := \mathbf{A} - \frac{1}{3}\text{tr}(\mathbf{A})\mathbf{1}$. A scalar product of two second-rank tensors is denoted by $\mathbf{A} : \mathbf{B} = \text{tr}(\mathbf{A} \mathbf{B}^T)$. This scalar product gives rise to the Frobenius norm $\|\mathbf{A}\| := \sqrt{\mathbf{A} : \mathbf{A}}$. For a certain material particle, the material time derivative is denoted by dot: $\dot{\mathbf{A}} := \frac{d}{dt}\mathbf{A}$, with the particle held fixed during differentiation.

2. Material model

2.1. Finite strain kinematics

In many cases, the consideration of rheological analogies provides insight into the main assumptions of material modeling (Reiner , 1960; Krawietz , 1986; Palmov , 1998, 2008). As a starting point, we consider the rheological model shown in Fig. 1. This model represents a modified Schvedoff element connected in series with an idealized porosity element.² The modified Schvedoff element exhibits nonlinear phenomena which are similar to plasticity with Bauschinger effect (Lion , 2000; Shutov and Kreißig , 2008a). The porosity element is introduced to account for the effect of damage-induced volume change, which is important for the correct prediction of hydrostatic component of stress.

In this paper we consider a system of constitutive equations which qualitatively reproduces the rheological model. Following the procedure described by Lion (2000), the displacements and forces in rheological elements are formally replaced by strains and stresses. Any connection of rheological elements in series will be represented by a multiplicative split of certain tensor-valued quantities.³ Let \mathbf{F} be the deformation gradient from the local reference configuration $\tilde{\mathcal{K}}$ to the

²Note that this rheological model has a similar structure to that of thermoplasticity with kinematic hardening (Lion , 2000; Shutov and Ihlemann , 2011). In the current study, the element of thermal expansion is replaced by the porosity element.

³This technique can be successfully adopted even for two-dimensional rheological elements (Shutov et al. , 2011). For a general framework dealing with one-dimensional rheological elements, we refer the reader to Bröcker and Matzenmiller (2014).

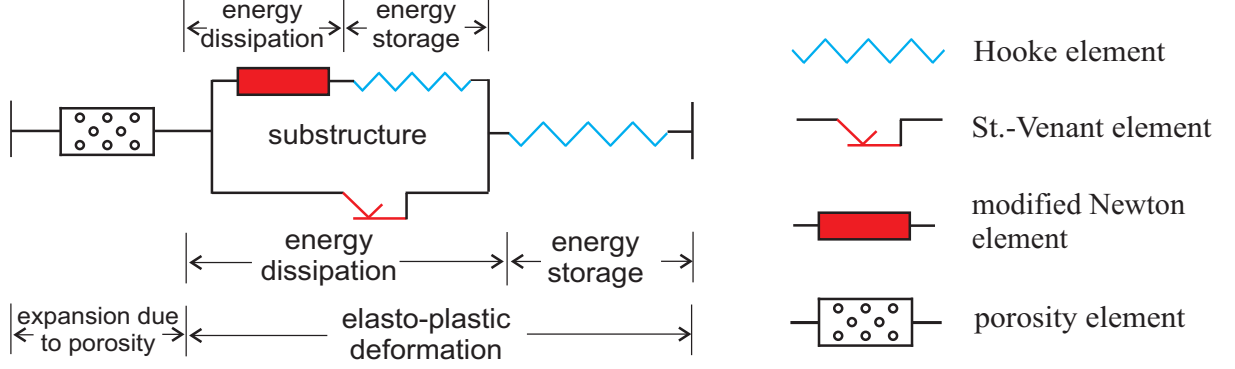


Figure 1: Rheological analogy: The model consists of an idealized porosity element connected in series with the modified Schwedoff element. The modified Schwedoff element is build up of two elastic springs (Hooke elements), one friction element (St.-Venant element), and a rate-independent dashpot (modified Newton element).

current configuration \mathcal{K} (see Fig. 2).⁴ First, we decompose it into an elasto-plastic part $\mathbf{F}_{\text{ep}}^{\text{por}}$ and a porosity-induced expansion \mathbf{F}_{por} in the following way

$$\mathbf{F} = \mathbf{F}_{\text{ep}}^{\text{por}} \mathbf{F}_{\text{por}}, \quad \mathbf{F}_{\text{por}} = \Phi^{1/3} \mathbf{1}, \quad \Phi \geq 1. \quad (1)$$

Following Bammann and Aifantis (1989), the expansion \mathbf{F}_{por} is assumed to be isotropic, where the damage-induced volume change is given by Φ

$$\det \mathbf{F}_{\text{por}} = \Phi. \quad (2)$$

The decomposition (1)₁ yields a configuration of porous material $\mathcal{K}^{\text{por}} := \mathbf{F}_{\text{por}} \mathcal{K}$. Let ρ_{R} be the mass density in the reference configuration. The mass density of unstressed porous material is given by $\rho_{\text{por}} := \rho_{\text{R}} / \Phi$. Next, we consider the well-known decomposition of the elasto-plastic part into an inelastic part $\mathbf{F}_{\text{i}}^{\text{por}}$ and an elastic part $\hat{\mathbf{F}}_{\text{e}}$

$$\mathbf{F}_{\text{ep}}^{\text{por}} = \hat{\mathbf{F}}_{\text{e}} \mathbf{F}_{\text{i}}^{\text{por}}. \quad (3)$$

Remark 1. Originally, this decomposition was motivated for metallic materials by the idea of elastic unloading to a stress-free state (Bilby et al. , 1957). In general, a pure elastic unloading is not possible and the multiplicative decomposition (3) becomes a constitutive assumption. There are some alternative ways to split the deformation into elastic and plastic parts, including the additive split of the strain rate (Xiao et al. , 2006). It is worth mentioning that the multiplicative decomposition brings the advantage of the so-called weak invariance of constitutive equations (Shutov and Ihlemann , 2014). \square

Following the approach of Lion (2000) to the nonlinear kinematic hardening, we decompose the inelastic part into a dissipative part $\mathbf{F}_{\text{ii}}^{\text{por}}$ and a conservative part $\check{\mathbf{F}}_{\text{ie}}$

$$\mathbf{F}_{\text{i}}^{\text{por}} = \check{\mathbf{F}}_{\text{ie}} \mathbf{F}_{\text{ii}}^{\text{por}}. \quad (4)$$

⁴A general introduction to the kinematics within the geometrically exact setting can be found in Khan and Huang (1995); Haupt (2002); Hashiguchi and Yamakawa (2012).

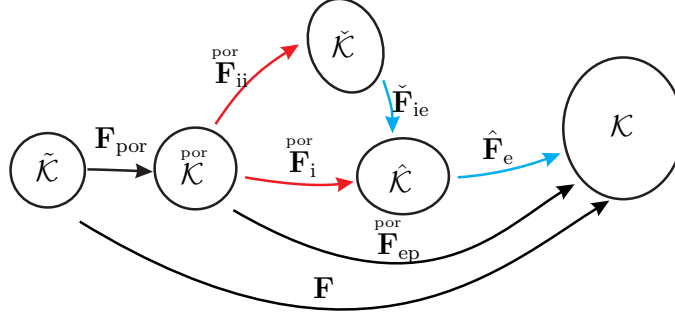


Figure 2: Commutative diagram: triple multiplicative decomposition of the deformation gradient.

We adopt this decomposition as a phenomenological assumption, without explicit discussion of its microstructural origins (Clayton et al. , 2014). Intuitively, one can relate the dissipative parts $\overset{\text{por}}{\mathbf{F}}_{\text{i}}$ and $\overset{\text{por}}{\mathbf{F}}_{\text{ii}}$ to the deformations of the St.-Venant element and the modified Newton element, respectively (cf. Fig. 1). The conservative parts $\hat{\mathbf{F}}_{\text{e}}$ and $\tilde{\mathbf{F}}_{\text{ie}}$ are associated with the deformation of the elastic springs (cf. Fig. 1). The commutative diagram shown in Fig. 2 is useful to summarize the introduced multiplicative decompositions. The fictitious local configurations $\hat{\mathcal{K}}$ and $\tilde{\mathcal{K}}$ are referred to as stress-free intermediate configuration and configuration of kinematic hardening, respectively.

Remark 2. Combining (1)₁ and (3) we arrive at

$$\mathbf{F} = \hat{\mathbf{F}}_{\text{e}} \overset{\text{por}}{\mathbf{F}}_{\text{i}} \mathbf{F}_{\text{por}}. \quad (5)$$

Due to the isotropy of \mathbf{F}_{por} , this decomposition is equivalent to the decomposition considered by Bammann and Aifantis (1989); Ahad et al. (2014) and many others:

$$\mathbf{F} = \hat{\mathbf{F}}_{\text{e}} \mathbf{F}_{\text{por}} \overset{\text{por}}{\mathbf{F}}_{\text{i}}. \quad (6)$$

In this paper we prefer to operate with (5) rather than (6) in order to retain the structure of the viscoplasticity model proposed by Shutov and Kreißig (2008a). \square

Remark 3. Note that only a volumetric part of damage kinematics is explicitly captured by \mathbf{F}_{por} in this study. Within a refined approach with enriched kinematic description, the damage-induced isochoric deformation can be also considered explicitly. It can be carried out through additional decomposition of the inelastic part $\overset{\text{por}}{\mathbf{F}}_{\text{i}}$ into some isochoric damage-induced parts and isochoric damage-free parts (cf. Voyiadjis and Park (1999); Brünig (2003)). Obviously, such an approach leads to an anisotropic damage model. \square

Remark 4. There exists an abundance of literature considering ductile damage modeling within multiplicative elasto-plasticity based on the split (3) (see, for example, Bammann and Aifantis (1989); Steinmann et al. (1994); Menzel et al. (2005); Soyarslan and Tekkaya (2010); Bammann and Solanki (2010), McAuliffe and Waisman (2015)). Unfortunately, only few damage models incorporate the multiplicative split (4) which is used to capture the nonlinear kinematic hardening. For instance, Grammenoudis et al. (2009); Bröcker and Matzenmiller (2014) have coupled ductile damage with a model of finite strain

plasticity by adopting the concept of effective stresses combined with the strain equivalence principle. Unfortunately, as will be seen from the following, such an approach is too restrictive in some cases. In particular, it implies that different hardening mechanisms deteriorate with the same rate for progressive damage, which is in general not true (see Section 4). Moreover, as already mentioned above, the damage-induced volume change has to be explicitly taken into account for accurate prediction of the hydrostatic component of stress. \square

Let us consider the right Cauchy-Green tensor (RCGT) $\mathbf{C} := \mathbf{F}^T \mathbf{F}$. Based on the decompositions (1)₁ and (3), we introduce the following kinematic quantities of the right Cauchy-Green type

$$\overset{\text{por}}{\mathbf{C}}_{\text{ep}} := \overset{\text{por}}{\mathbf{F}}_{\text{ep}}^T \overset{\text{por}}{\mathbf{F}}_{\text{ep}}, \quad \overset{\text{por}}{\mathbf{C}}_{\text{i}} := \overset{\text{por}}{\mathbf{F}}_{\text{i}}^T \overset{\text{por}}{\mathbf{F}}_{\text{i}}, \quad \hat{\mathbf{C}}_{\text{e}} := \hat{\mathbf{F}}_{\text{e}}^T \hat{\mathbf{F}}_{\text{e}}. \quad (7)$$

Here, the elasto-plastic RCGT $\overset{\text{por}}{\mathbf{C}}_{\text{ep}}$ and the inelastic RCGT $\overset{\text{por}}{\mathbf{C}}_{\text{i}}$ operate on the porous configuration $\overset{\text{por}}{\mathcal{K}}$; the elastic RCGT $\hat{\mathbf{C}}_{\text{e}}$ operates on the stress-free configuration $\hat{\mathcal{K}}$. Next, on the basis of decomposition (4), we define the inelastic RCGT of substructure $\overset{\text{por}}{\mathbf{C}}_{\text{ii}}$ and the elastic RCGT of substructure $\check{\mathbf{C}}_{\text{ie}}$

$$\overset{\text{por}}{\mathbf{C}}_{\text{ii}} := \overset{\text{por}}{\mathbf{F}}_{\text{ii}}^T \overset{\text{por}}{\mathbf{F}}_{\text{ii}}, \quad \check{\mathbf{C}}_{\text{ie}} := \check{\mathbf{F}}_{\text{ie}}^T \check{\mathbf{F}}_{\text{ie}}. \quad (8)$$

The tensors $\overset{\text{por}}{\mathbf{C}}_{\text{ii}}$ and $\check{\mathbf{C}}_{\text{ie}}$ operate on $\overset{\text{por}}{\mathcal{K}}$ and $\check{\mathcal{K}}$ respectively. Combining (1) and (7)₁, we have

$$\overset{\text{por}}{\mathbf{C}}_{\text{ep}} = \Phi^{-2/3} \mathbf{C}. \quad (9)$$

In order to describe the inelastic flow we consider the inelastic velocity gradient $\hat{\mathbf{L}}_{\text{i}}$ and the inelastic strain rate $\hat{\mathbf{D}}_{\text{i}}$, both operating on $\hat{\mathcal{K}}$

$$\hat{\mathbf{L}}_{\text{i}} := \left(\frac{d}{dt} \overset{\text{por}}{\mathbf{F}}_{\text{i}} \right) \overset{\text{por}}{\mathbf{F}}_{\text{i}}^{-1}, \quad \hat{\mathbf{D}}_{\text{i}} := \text{sym}(\hat{\mathbf{L}}_{\text{i}}). \quad (10)$$

Analogously, the inelastic flow of the substructure is captured using the following tensors operating on $\check{\mathcal{K}}$

$$\check{\mathbf{L}}_{\text{ii}} := \left(\frac{d}{dt} \overset{\text{por}}{\mathbf{F}}_{\text{ii}} \right) \overset{\text{por}}{\mathbf{F}}_{\text{ii}}^{-1}, \quad \check{\mathbf{D}}_{\text{ii}} := \text{sym}(\check{\mathbf{L}}_{\text{ii}}). \quad (11)$$

In terms of the rheological analogy shown in Fig. 1, the strain rates $\hat{\mathbf{D}}_{\text{i}}$ and $\check{\mathbf{D}}_{\text{ii}}$ can be associated with the deformation rates of the St.-Venant element and the modified Newton element, respectively.

The accumulated inelastic arc-length (Odqvist parameter) is a strain-like internal variable defined through

$$s(t) := \int_0^t \dot{s}(\tau) d\tau, \quad \dot{s} := \sqrt{\frac{2}{3}} \|\hat{\mathbf{D}}_{\text{i}}\|. \quad (12)$$

Along with s we introduce its dissipative part s_{d} such that $s_{\text{e}} := s - s_{\text{d}}$ controls the isotropic hardening.⁵

⁵ For simplicity, the rheological model in Fig. 1 does not include the isotropic hardening. The reader interested in idealized rheological elements of isotropic hardening is referred to Bröcker and Matzenmiller (2013).

2.2. Stresses

Let \mathbf{T} and $\mathbf{S} := \det(\mathbf{F})\mathbf{T}$ be respectively the Cauchy and Kirchhoff stresses. We introduce a Kirchhoff-like stress tensor operating on the current configuration \mathcal{K}

$$\mathbf{S}_{\text{ep}} := \det(\overset{\text{por}}{\mathbf{F}}_{\text{ep}})\mathbf{T} = \Phi^{-1}\mathbf{S}. \quad (13)$$

The elastic pull-back of this tensor yields its counterpart operating on the stress-free configuration $\hat{\mathcal{K}}$

$$\hat{\mathbf{S}}_{\text{ep}} := \hat{\mathbf{F}}_{\text{e}}^{-1}\mathbf{S}_{\text{ep}}\hat{\mathbf{F}}_{\text{e}}^{-\text{T}}. \quad (14)$$

The 2nd Piola-Kirchhoff tensor is obtained applying a pull-back to \mathbf{S}

$$\tilde{\mathbf{T}} := \mathbf{F}^{-1}\mathbf{S}\mathbf{F}^{-\text{T}}. \quad (15)$$

Analogously, the elasto-plastic pull-back of \mathbf{S}_{ep} yields a Kirchhoff-like tensor operating on the porous configuration $\overset{\text{por}}{\mathcal{K}}$. At the same time, this tensor is identical to the inelastic pull-back of $\hat{\mathbf{S}}_{\text{ep}}$:

$$\overset{\text{por}}{\mathbf{T}}_{\text{ep}} := \overset{\text{por}}{\mathbf{F}}_{\text{ep}}^{-1}\mathbf{S}_{\text{ep}}\overset{\text{por}}{\mathbf{F}}_{\text{ep}}^{-\text{T}} = \overset{\text{por}}{\mathbf{F}}_{\text{i}}^{-1}\hat{\mathbf{S}}_{\text{ep}}\overset{\text{por}}{\mathbf{F}}_{\text{i}}^{-\text{T}}. \quad (16)$$

The stress tensors $\tilde{\mathbf{T}}$ and $\overset{\text{por}}{\mathbf{T}}_{\text{ep}}$ are related by

$$\tilde{\mathbf{T}} = \Phi^{1/3}\overset{\text{por}}{\mathbf{T}}_{\text{ep}}. \quad (17)$$

Next, let us consider the backstresses which are typically used to capture the Bauschinger effect.⁶ Intuitively, the backstresses correspond to stresses in the modified Newton element which is a part of the Schwedoff element shown in Fig. 1. Let $\check{\mathbf{X}}$ be the backstress operating on $\check{\mathcal{K}}$, which is a stress measure power-conjugate to the strain rate $\check{\mathbf{D}}_{\text{ii}}$. A backstress measure operating on the stress-free configuration $\hat{\mathcal{K}}$ is obtained using a push-forward operation as follows

$$\hat{\mathbf{X}} := \check{\mathbf{F}}_{\text{ie}}\check{\mathbf{X}}\check{\mathbf{F}}_{\text{ie}}^{\text{T}}. \quad (18)$$

Its counterpart operating on the porous configuration $\overset{\text{por}}{\mathcal{K}}$ is given by

$$\overset{\text{por}}{\mathbf{X}} := \overset{\text{por}}{\mathbf{F}}_{\text{ii}}^{-1}\check{\mathbf{X}}\overset{\text{por}}{\mathbf{F}}_{\text{ii}}^{-\text{T}} = \overset{\text{por}}{\mathbf{F}}_{\text{i}}^{-1}\hat{\mathbf{X}}\overset{\text{por}}{\mathbf{F}}_{\text{i}}^{-\text{T}}. \quad (19)$$

A Mandel-like backstress tensor on $\check{\mathcal{K}}$ is defined through

$$\check{\mathbf{\Xi}} := \check{\mathbf{C}}_{\text{ie}}\check{\mathbf{X}}. \quad (20)$$

For what follows, it is instructive to introduce the so-called effective stress operating on $\hat{\mathcal{K}}$

$$\hat{\mathbf{\Sigma}} := \hat{\mathbf{C}}_{\text{e}}\hat{\mathbf{S}}_{\text{ep}} - \hat{\mathbf{X}}. \quad (21)$$

⁶A backstresses-free approach to the Bauschinger effect was presented by Barlat et al. (2011).

In other words, the effective stress represents the difference between the Mandel-like stress $\hat{\mathbf{C}}_e \hat{\mathbf{S}}_{ep}$ and the backstress $\hat{\mathbf{X}}$. For this definition, a Kirchhoff-like stress \mathbf{S}_{ep} is adopted instead of the Kirchhoff stress \mathbf{S} in order to keep the structure of the damage model close to the viscoplasticity model presented by Shutov and Kreiig (2008a). The effective stress represents the local force driving the inelastic deformation. In terms of the rheological model, this stress corresponds to the load acting on the St.-Venant element.⁷

2.3. Free energy

According to Tvergaard (1989), the scalar porosity parameter is an adequate damage measure at the initial stage of ductile damage process. Only small pore volume fractions will be considered in this paper, such that the applicability domain of the model is restricted to $\Phi - 1 \ll 1$. The material porosity will be seen as a rough measure of damage (cf. also Bammann and Aifantis (1989)). Aiming at a thermodynamically consistent formulation, we postulate the free energy per unit mass in the form

$$\psi = \psi(\hat{\mathbf{C}}_e, \check{\mathbf{C}}_{ie}, s_e, \Phi) = \psi_{el}(\hat{\mathbf{C}}_e, \Phi) + \psi_{kin}(\check{\mathbf{C}}_{ie}, \Phi) + \psi_{iso}(s_e, \Phi), \quad (22)$$

where ψ_{el} corresponds to the energy stored due to macroscopic elastic deformations, components ψ_{kin} and ψ_{iso} correspond to the energy storage associated with kinematic and isotropic hardening.⁸ The dependence of ψ_{el} , ψ_{kin} , and ψ_{iso} on Φ is introduced in order to capture the damage-induced deterioration of elastic and hardening properties, as is common for metals. In this study, the system of constitutive equations will be formulated in case of general isotropic energy-storage functions $\psi_{el}(\hat{\mathbf{C}}_e, \Phi)$ and $\psi_{kin}(\check{\mathbf{C}}_{ie}, \Phi)$. However, some concrete assumptions will be needed for the numerical computations. To be definite, we postulate

$$\rho_R \psi_{el}(\hat{\mathbf{C}}_e, \Phi) = \frac{k(\Phi)}{2} (\ln \sqrt{\det \hat{\mathbf{C}}_e})^2 + \frac{\mu(\Phi)}{2} (\text{tr} \overline{\hat{\mathbf{C}}_e} - 3), \quad (23)$$

$$\rho_R \psi_{kin}(\check{\mathbf{C}}_{ie}, \Phi) = \frac{c(\Phi)}{4} (\text{tr} \overline{\check{\mathbf{C}}_{ie}} - 3), \quad \rho_R \psi_{iso}(s_e) = \frac{\gamma(\Phi)}{2} (s_e)^2, \quad (24)$$

where the overline $\overline{(\cdot)}$ denotes the unimodular part of a second-rank tensor

$$\overline{\mathbf{A}} := (\det \mathbf{A})^{-1/3} \mathbf{A}. \quad (25)$$

Although the elastic properties of the damaged material remain isotropic, different deterioration rates have to be introduced for the bulk modulus $k(\Phi)$ and the shear modulus $\mu(\Phi)$ (Bristow , 1960)

$$k(\Phi) = k_0 \exp(-\text{BRR} \cdot (\Phi - 1)), \quad \mu(\Phi) = \mu_0 \exp(-\text{SRR} \cdot (\Phi - 1)). \quad (26)$$

⁷ A distinction should be made between the effective stress concept which is typically used in continuum damage mechanics (Rabotnov , 1969) and the notion of effective stress adopted within plasticity with kinematic hardening. In fact, the second notion is implemented in the current study with respect to $\hat{\mathbf{\Sigma}}$.

⁸ More precisely, $\psi_{kin} + \psi_{iso}$ is a part of the free energy stored in the defects of the crystal structure. Remaining parts of the ‘‘defect energy’’ which are detached from any hardening mechanism (Shutov and Ihlemann , 2011) are neglected here. An accurate description of the energy storage becomes especially important within thermoplasticity with nonlinear kinematic hardening (Canadija and Brnic , 2004; Canadija and Mosler , 2011; Shutov and Ihlemann , 2011).

Here, constant parameters $\text{BRR} \geq 0$ and $\text{SRR} \geq 0$ stand for “bulk reduction rate” and “shear reduction rate” respectively. The assumption (26) can reproduce the experimentally observed decrease of Poisson’s ratio. Analogously, for the degradation of the hardening mechanisms we postulate

$$c(\Phi) = c_0 \exp(-\text{KRR} \cdot (\Phi - 1)), \quad \gamma(\Phi) = \gamma_0 \exp(-\text{IRR} \cdot (\Phi - 1)), \quad (27)$$

with $\text{KRR} \geq 0$ and $\text{IRR} \geq 0$. Here, the parameter KRR stands for “kinematic hardening reduction rate”, and IRR for “isotropic hardening reduction rate”.

As follows from (26) and (27), the material parameters $k_0 > 0$, $\mu_0 > 0$, $c_0 > 0$, and $\gamma_0 > 0$ correspond to the reference state with $\Phi = 1$.

Remark 5. Even for $k = \text{const}$ and $\mu = \text{const}$, a weak damage-elasticity coupling is predicted by (23) due to the mass density reduction. This type of weak coupling is also exhibited by the well-known Rousselier model (cf., for example, Rousselier (1987)). \square

Now we introduce the following relations of hyperelastic type which express the stresses $\hat{\mathbf{S}}_{\text{ep}}$, the backstresses $\check{\mathbf{X}}$, and the isotropic hardening R as a function of introduced kinematic variables

$$\hat{\mathbf{S}}_{\text{ep}} = 2\rho_{\text{por}} \frac{\partial \psi_{\text{el}}(\hat{\mathbf{C}}_e, \Phi)}{\partial \hat{\mathbf{C}}_e}, \quad \check{\mathbf{X}} = 2\rho_{\text{por}} \frac{\partial \psi_{\text{kin}}(\check{\mathbf{C}}_{\text{ie}}, \Phi)}{\partial \check{\mathbf{C}}_{\text{ie}}}, \quad R = \rho_{\text{por}} \frac{\partial \psi_{\text{iso}}(s_e, \Phi)}{\partial s_e}. \quad (28)$$

The relations (28)₁ and (28)₂ can be motivated by the rheological model shown in Fig. (1), if a hyperelastic response is assumed for both elastic springs. On the other hand, these relations will play a crucial role in the proof of the thermodynamic consistency (cf. Section 2.4). Another implication of (28) is that $(\hat{\mathbf{S}}_{\text{ep}}, \hat{\mathbf{C}}_e)$, $(\check{\mathbf{X}}, \check{\mathbf{C}}_{\text{ie}})$, and (R, s_e) form conjugate pairs. Originally, a hyperelastic relation similar to (28)₁ was introduced by Simo and Ortiz (1985). The advantage of such approach is that a truly hyperelastic behavior is obtained in the elastic range and the principle of objectivity is trivially satisfied.

2.4. Clausius-Duhem inequality

Here we consider the Clausius-Duhem inequality, which states that the internal dissipation δ_i is always non-negative. For isothermal processes studied in this paper, this inequality takes the reduced form (cf., for instance, Haupt (2002))

$$\delta_i := \frac{1}{\rho_R} \tilde{\mathbf{T}} : \dot{\mathbf{E}} - \dot{\psi} \geq 0. \quad (29)$$

Let us specialize this inequality for the free energy given by (22). First, we decompose the stress power into a power of the hydrostatic stress component on the damage-induced volume expansion and the remaining part⁹

$$\frac{1}{\rho_R} \tilde{\mathbf{T}} : \dot{\mathbf{E}} = \frac{1}{\rho_{\text{por}}} \left(\frac{\dot{\Phi}}{3\Phi} \mathbf{T}_{\text{ep}}^{\text{por}} : \mathbf{C}_{\text{ep}}^{\text{por}} + \mathbf{T}_{\text{ep}}^{\text{por}} : \frac{1}{2} \dot{\mathbf{C}}_{\text{ep}}^{\text{por}} \right). \quad (30)$$

⁹A similar decomposition is obtained for some models of thermoplasticity due to the similar description of kinematics (Lion, 2000; Shutov and Ihlemann, 2011).

Recalling (9) and (17) we obtain the following relation for the hydrostatic stress component

$$\mathbf{T}_{\text{ep}}^{\text{por}} : \mathbf{C}_{\text{ep}}^{\text{por}} = \Phi^{-1} \tilde{\mathbf{T}} : \mathbf{C}. \quad (31)$$

Let us take a closer look at the stress power $\mathbf{T}_{\text{ep}}^{\text{por}} : \frac{1}{2} \dot{\mathbf{C}}_{\text{ep}}^{\text{por}}$. As is usually done in multiplicative inelasticity (cf. equation (2.28) in Lion (2000) or equation (13.258) in Haupt (2002)), this quantity is split into two components. More precisely, it follows from (3) that

$$\mathbf{T}_{\text{ep}}^{\text{por}} : \frac{1}{2} \dot{\mathbf{C}}_{\text{ep}}^{\text{por}} = \hat{\mathbf{S}}_{\text{ep}} : \frac{1}{2} \dot{\hat{\mathbf{C}}}_{\text{e}} + (\hat{\mathbf{C}}_{\text{e}} \hat{\mathbf{S}}_{\text{ep}}) : \hat{\mathbf{L}}_{\text{i}}. \quad (32)$$

Since ψ_{el} is isotropic, relation (28)₁ implies that the tensors $\hat{\mathbf{C}}_{\text{e}}$ and $\hat{\mathbf{S}}_{\text{ep}}$ commute. In that case, the Mandel tensor $\hat{\mathbf{C}}_{\text{e}} \hat{\mathbf{S}}_{\text{ep}}$ is symmetric and (32) yields

$$\mathbf{T}_{\text{ep}}^{\text{por}} : \frac{1}{2} \dot{\mathbf{C}}_{\text{ep}}^{\text{por}} = \hat{\mathbf{S}}_{\text{ep}} : \frac{1}{2} \dot{\hat{\mathbf{C}}}_{\text{e}} + (\hat{\mathbf{C}}_{\text{e}} \hat{\mathbf{S}}_{\text{ep}}) : \hat{\mathbf{D}}_{\text{i}}. \quad (33)$$

Next, it follows from (28)₂ that $\check{\mathbf{C}}_{\text{ie}}$ and $\check{\mathbf{X}}$ commute as a result of the isotropy assumption made for ψ_{kin} . Therefore, the Mandel-like tensor $\check{\mathbf{\Xi}} = \check{\mathbf{C}}_{\text{ie}} \check{\mathbf{X}}$ is symmetric. Taking the multiplicative split (4) into account, we obtain a relation for the backstress power, which has a similar structure to (33)

$$\hat{\mathbf{X}} : \hat{\mathbf{D}}_{\text{i}} = \check{\mathbf{X}} : \frac{1}{2} \dot{\check{\mathbf{C}}}_{\text{ie}} + (\check{\mathbf{C}}_{\text{ie}} \check{\mathbf{X}}) : \check{\mathbf{D}}_{\text{ii}}. \quad (34)$$

Rearranging the terms, we arrive at

$$0 = -\hat{\mathbf{X}} : \hat{\mathbf{D}}_{\text{i}} + \check{\mathbf{X}} : \frac{1}{2} \dot{\check{\mathbf{C}}}_{\text{ie}} + (\check{\mathbf{C}}_{\text{ie}} \check{\mathbf{X}}) : \check{\mathbf{D}}_{\text{ii}}. \quad (35)$$

Summing both sides of (33) and (35) we obtain the stress power as

$$\mathbf{T}_{\text{ep}}^{\text{por}} : \frac{1}{2} \dot{\mathbf{C}}_{\text{ep}}^{\text{por}} = \hat{\mathbf{S}}_{\text{ep}} : \frac{1}{2} \dot{\hat{\mathbf{C}}}_{\text{e}} + (\hat{\mathbf{C}}_{\text{e}} \hat{\mathbf{S}}_{\text{ep}}) : \hat{\mathbf{D}}_{\text{i}} - \hat{\mathbf{X}} : \hat{\mathbf{D}}_{\text{i}} + \check{\mathbf{X}} : \frac{1}{2} \dot{\check{\mathbf{C}}}_{\text{ie}} + (\check{\mathbf{C}}_{\text{ie}} \check{\mathbf{X}}) : \check{\mathbf{D}}_{\text{ii}}. \quad (36)$$

On the other hand, for the rate of the free energy we have

$$\dot{\psi} \stackrel{(22)}{=} \frac{\partial \psi_{\text{el}}(\hat{\mathbf{C}}_{\text{e}}, \Phi)}{\partial \hat{\mathbf{C}}_{\text{e}}} : \dot{\hat{\mathbf{C}}}_{\text{e}} + \frac{\partial \psi_{\text{kin}}(\check{\mathbf{C}}_{\text{ie}}, \Phi)}{\partial \check{\mathbf{C}}_{\text{ie}}} : \dot{\check{\mathbf{C}}}_{\text{ie}} + \frac{\partial \psi_{\text{iso}}(s_{\text{e}}, \Phi)}{\partial s_{\text{e}}} \dot{s}_{\text{e}} + \frac{\partial \psi(\hat{\mathbf{C}}_{\text{e}}, \check{\mathbf{C}}_{\text{ie}}, s_{\text{e}}, \Phi)}{\partial \Phi} \dot{\Phi}. \quad (37)$$

Substituting (30) and (37) into (29) and taking (36) into account we rewrite the internal dissipation in the form

$$\begin{aligned} \delta_{\text{i}} = & \left(\frac{1}{\rho_{\text{por}}} \frac{1}{3\Phi} \mathbf{T}_{\text{ep}}^{\text{por}} : \mathbf{C}_{\text{ep}}^{\text{por}} - \frac{\partial \psi(\hat{\mathbf{C}}_{\text{e}}, \check{\mathbf{C}}_{\text{ie}}, s_{\text{e}}, \Phi)}{\partial \Phi} \right) \dot{\Phi} + \left(\frac{1}{2\rho_{\text{por}}} \hat{\mathbf{S}}_{\text{ep}} - \frac{\partial \psi_{\text{el}}(\hat{\mathbf{C}}_{\text{e}}, \Phi)}{\partial \hat{\mathbf{C}}_{\text{e}}} \right) : \dot{\hat{\mathbf{C}}}_{\text{e}} \\ & + \left(\frac{1}{2\rho_{\text{por}}} \check{\mathbf{X}} - \frac{\partial \psi_{\text{kin}}(\check{\mathbf{C}}_{\text{ie}}, \Phi)}{\partial \check{\mathbf{C}}_{\text{ie}}} \right) : \dot{\check{\mathbf{C}}}_{\text{ie}} + \frac{1}{\rho_{\text{por}}} (\hat{\mathbf{C}}_{\text{e}} \hat{\mathbf{S}}_{\text{ep}} - \hat{\mathbf{X}}) : \hat{\mathbf{D}}_{\text{i}} + \frac{1}{\rho_{\text{por}}} (\check{\mathbf{C}}_{\text{ie}} \check{\mathbf{X}}) : \check{\mathbf{D}}_{\text{ii}} \\ & - \frac{\partial \psi_{\text{iso}}(s_{\text{e}}, \Phi)}{\partial s_{\text{e}}} \dot{s}_{\text{e}}. \end{aligned} \quad (38)$$

Taking the potential relations (28) into account and recalling the abbreviations (20), (21), the internal dissipation takes the following simple form

$$\delta_i = \left(\frac{1}{\rho_{\text{por}}} \frac{1}{3\Phi} \mathbf{T}_{\text{ep}}^{\text{por}} : \mathbf{C}_{\text{ep}}^{\text{por}} - \frac{\partial \psi(\hat{\mathbf{C}}_e, \check{\mathbf{C}}_{\text{ie}}, s_e, \Phi)}{\partial \Phi} \right) \dot{\Phi} + \frac{1}{\rho_{\text{por}}} (\hat{\Sigma} : \hat{\mathbf{D}}_i + \check{\Xi} : \check{\mathbf{D}}_{\text{ii}} - R\dot{s}_e). \quad (39)$$

Damage-induced energy dissipation is given by the first term on the right-hand side of (39). The remaining part corresponds to the energy dissipation induced by isochoric plasticity. In other words, this relation encompasses the concept that both plasticity and damage are dissipative processes. As a sufficient condition for the Clausius-Duhem inequality, we assume that both contributions are non-negative

$$\delta_i^{\text{damage}} := \left(\frac{1}{\rho_{\text{por}}} \frac{1}{3\Phi} \mathbf{T}_{\text{ep}}^{\text{por}} : \mathbf{C}_{\text{ep}}^{\text{por}} - \frac{\partial \psi(\hat{\mathbf{C}}_e, \check{\mathbf{C}}_{\text{ie}}, s_e, \Phi)}{\partial \Phi} \right) \dot{\Phi} \geq 0, \quad (40)$$

$$\delta_i^{\text{plasticity}} := \frac{1}{\rho_{\text{por}}} ((\hat{\Sigma} : \hat{\mathbf{D}}_i - R\dot{s}) + \check{\Xi} : \check{\mathbf{D}}_{\text{ii}} + R\dot{s}_d) \geq 0. \quad (41)$$

Note that the terms $\hat{\Sigma} : \hat{\mathbf{D}}_i$ and $\check{\Xi} : \check{\mathbf{D}}_{\text{ii}}$ are related to the energy dissipation in the friction element and the rate-independent dashpot, shown in Fig. 1.

2.5. Yield condition and evolution equations

Ductile damage influences both the plastic flow and the size of the elastic domain in the stress space. To account for these effects, we consider the yield function as follows

$$f := \|\hat{\Sigma}^{\text{D}}\| - \sqrt{\frac{2}{3}} [K(\Phi) + R], \quad (42)$$

where $K(\Phi) \geq 0$ stands for the damage-dependent yield stress. As a sufficient condition for the inequality (41), we postulate the following evolution equations for the inelastic flow and the inelastic flow of the substructure

$$\hat{\mathbf{D}}_i = \lambda_i \frac{\hat{\Sigma}^{\text{D}}}{\|\hat{\Sigma}^{\text{D}}\|}, \quad \check{\mathbf{D}}_{\text{ii}} = \lambda_i \varkappa(\Phi) \check{\Xi}^{\text{D}}, \quad (43)$$

$$\dot{s} = \sqrt{\frac{2}{3}} \lambda_i, \quad \dot{s}_d = \frac{\beta(\Phi)}{\gamma(\Phi)} \dot{s} R, \quad (44)$$

where $\varkappa(\Phi) \geq 0$ and $\beta(\Phi) \geq 0$ are damage-dependent hardening parameters and $\lambda_i \geq 0$ is the inelastic multiplier. It was shown by Shutov et al. (2013) (Section 2.2) that the flow rule (43)₁ corresponds to the flow rule previously formulated by Simo and Miehe (1992) on the current configuration. It follows from (43)₁ that $\lambda_i = \|\hat{\mathbf{D}}_i\|$. Thus, λ_i corresponds to the intensity of the inelastic flow. In this paper we describe it based on Peryzyna's rate-dependent overstress theory (Peryzyna, 1966)

$$\lambda_i = \frac{1}{\eta} \left\langle \frac{f}{f_0} \right\rangle^m, \quad \langle x \rangle := \max(x, 0). \quad (45)$$

Here, $f_0 > 0$ is used to obtain a non-dimensional term in the angle bracket.¹⁰ For simplicity, we assume that the viscosity parameters $\eta \geq 0$ and $m \geq 1$ are not affected by damage.

The evolution equation (43)₁ complies with the normality flow rule.¹¹ Both inelastic flows governed by (43) are incompressible. Indeed, after some computations we arrive at

$$\frac{d}{dt}(\det \mathbf{F}_i^{\text{por}}) = (\det \mathbf{F}_i^{\text{por}}) \operatorname{tr}(\hat{\mathbf{D}}_i) \stackrel{(43)_1}{=} 0, \quad \frac{d}{dt}(\det \mathbf{F}_{ii}^{\text{por}}) = (\det \mathbf{F}_{ii}^{\text{por}}) \operatorname{tr}(\check{\mathbf{D}}_{ii}) \stackrel{(43)_2}{=} 0. \quad (46)$$

Therefore, under appropriate initial conditions we have

$$\det \mathbf{F}_i^{\text{por}} = \det \mathbf{F}_{ii}^{\text{por}} = \det \mathbf{C}_i^{\text{por}} = \det \mathbf{C}_{ii}^{\text{por}} = 1. \quad (47)$$

In particular, the volume changes are accommodated by the elastic bulk strain and the damage-induced expansion of the material, but not by the inelastic deformation. Thus, $\det \mathbf{F} = \det \hat{\mathbf{F}}_e \Phi$.

Note that in case of constant $\gamma(\Phi)$ and $\beta(\Phi)$, the classical Voce rule of isotropic hardening is reproduced by (44)₂. In that case, the parameter β governs the saturation rate. For simplicity, we may postulate $\beta(\Phi) = \beta_0 = \text{const}$. A similar assumption for the kinematic hardening would imply

$$c(\Phi) \varkappa(\Phi) = \text{const} = c_0 \varkappa_0, \quad \varkappa(\Phi) \stackrel{(27)_1}{=} \varkappa_0 \exp(\text{KRR} \cdot (\Phi - 1)). \quad (48)$$

Moreover, we note that the yield stress $K(\Phi)$ is connected with the isotropic hardening of the material, since it appears in combination with R (cf. (42)). Therefore, it is natural to assume that $K(\Phi)$ is affected by damage in the same way as the isotropic hardening. More precisely, we assume¹²

$$K(\Phi) = K_0 \exp(-\text{IRR} \cdot (\Phi - 1)). \quad (49)$$

Within our framework, the damage evolution is postulated as a function of the inelastic strain rate $\hat{\mathbf{D}}_i$, the effective stress $\hat{\Sigma}$, the backstress $\hat{\mathbf{X}}$, and the damage variable Φ

$$\dot{\Phi} = \dot{\Phi}(\hat{\mathbf{D}}_i, \hat{\Sigma}, \hat{\mathbf{X}}, \Phi). \quad (50)$$

We consider ductile damage as a strain-driven process. Therefore, we suppose that $\dot{\Phi}$ is a homogeneous function of $\hat{\mathbf{D}}_i$

$$\dot{\Phi}(\alpha \hat{\mathbf{D}}_i, \hat{\Sigma}, \hat{\mathbf{X}}, \Phi) = \alpha \dot{\Phi}(\hat{\mathbf{D}}_i, \hat{\Sigma}, \hat{\mathbf{X}}, \Phi), \quad \text{for all } \alpha \geq 0. \quad (51)$$

It follows immediately from this relation that the damage does not evolve if the plastic flow is frozen. Next, for simplicity, we do not consider any material curing in this study. In combination with the inequality (40) we have the following restrictions

$$\dot{\Phi} \geq 0, \quad \dot{\Phi} = 0 \text{ for } \frac{1}{\rho_{\text{por}}} \frac{1}{3\Phi} \mathbf{T}_{\text{ep}}^{\text{por}} : \mathbf{C}_{\text{ep}}^{\text{por}} < \frac{\partial \psi(\hat{\mathbf{C}}_e, \check{\mathbf{C}}_{ie}, s_e, \Phi)}{\partial \Phi}. \quad (52)$$

¹⁰Thus, f_0 is not a material parameter.

¹¹We postulate that the porous material obeys the normality rule as soon as the normality rule holds true for the matrix material (Berg, 1969).

¹²This relation is reasonable for small pore volume fractions, which we assume in the current study. Numerical simulations performed by Fritzen et al. (2012) demonstrate that none of the classical yield conditions can predict the material yielding at pore volume fraction above 10%, and a refined constitutive modeling is needed.

Taking into account that $\frac{\partial \psi(\hat{\mathbf{C}}_e, \check{\mathbf{C}}_{ie}, s_e, \Phi)}{\partial \Phi} \leq 0$ (cf. Section 2.3), the restriction (52)₂ states that the damage-induced expansion is impossible whenever the hydrostatic pressure exceeds a certain limit. As it was pointed out by Bao and Wierzbicki (2005), fracture never occurs in some materials under very high hydrostatic pressure. It is impressive that a similar restriction is obtained here in a natural way as a sufficient condition for thermodynamic consistency.

Although the presented framework is based on phenomenological assumptions, the damage evolution law (50) provides an entry point for micromechanical approaches to damage modeling (cf. the comprehensive review by Besson (2010)). It may include the modeling of void nucleation, growth, and coalescence (some fundamental approaches are discussed by Marini et al. (1985); Pardoen and Hutchinson (2000); Xue (2007); Brüning et al. (2014)). Since the validation and calibration of such models requires certain microstructural observations, these models may be helpful *in extending the applicability range* of the purely phenomenological models. On the other hand, as emphasized by Hammi and Horstemeyer (2007), the calibration of physics-based *anisotropic* damage models is highly non-trivial: Taking the directional character of data for anisotropic analysis into account, some quantitative experimental data like void growth and coalescence are hardly measurable.

There is an abundance of literature dealing with specific fracture criteria (see, for example, Khan and Liu (2012) and references therein). Therefore this issue is not addressed in the present publication.

2.6. Void nucleation rule

Various void nucleation rules are available in the literature (cf. Appendix A). In this subsection we construct a new simple rule of void nucleation for porous ductile metals with second phases. Let N be the number of voids per unit volume of reference configuration. The nucleation rule is based on consideration of different nucleation mechanisms. We assume

$$\dot{N} = \dot{N}_{\text{tens}} + \dot{N}_{\text{shear}} + \dot{N}_{\text{comp}}, \quad (53)$$

where \dot{N}_{tens} and \dot{N}_{shear} stand for the nucleation rates due to separation of the matrix material under local tension and shear, respectively; \dot{N}_{comp} corresponds to the crushing of inclusions under local hydrostatic compression. It is assumed that void nucleation is driven by the inelastic flow (cf. Gurson (1977); Goods and Brown (1979)). Since the flow is governed by the effective stress tensor $\hat{\Sigma}$, a similar assumption is made for void nucleation, which is now controlled by the effective stress, and not by the total stress. Let σ_1 , σ_2 , and σ_3 be the eigenvalues of the effective stress $\hat{\Sigma}$. Additionally, we introduce the norm of its deviatoric part

$$\mathfrak{F} := \|\hat{\Sigma}^D\|. \quad (54)$$

We postulate the void nucleation rate under local tension as follows

$$\dot{N}_{\text{tens}} = n_{\text{tens}} \lambda_i \left\{ \left\langle \frac{\sigma_1}{\sqrt{3/2}\mathfrak{F}} - K_{\text{tens}} \right\rangle + \left\langle \frac{\sigma_2}{\sqrt{3/2}\mathfrak{F}} - K_{\text{tens}} \right\rangle + \left\langle \frac{\sigma_3}{\sqrt{3/2}\mathfrak{F}} - K_{\text{tens}} \right\rangle \right\}. \quad (55)$$

Here, the parameter $n_{\text{tens}} \geq 0$ controls the intensity of the void nucleation, $K_{\text{tens}} < 1$ represents a certain threshold and $\langle x \rangle = \max(x, 0)$. The distribution of the void nucleation rate \dot{N}_{tens} in

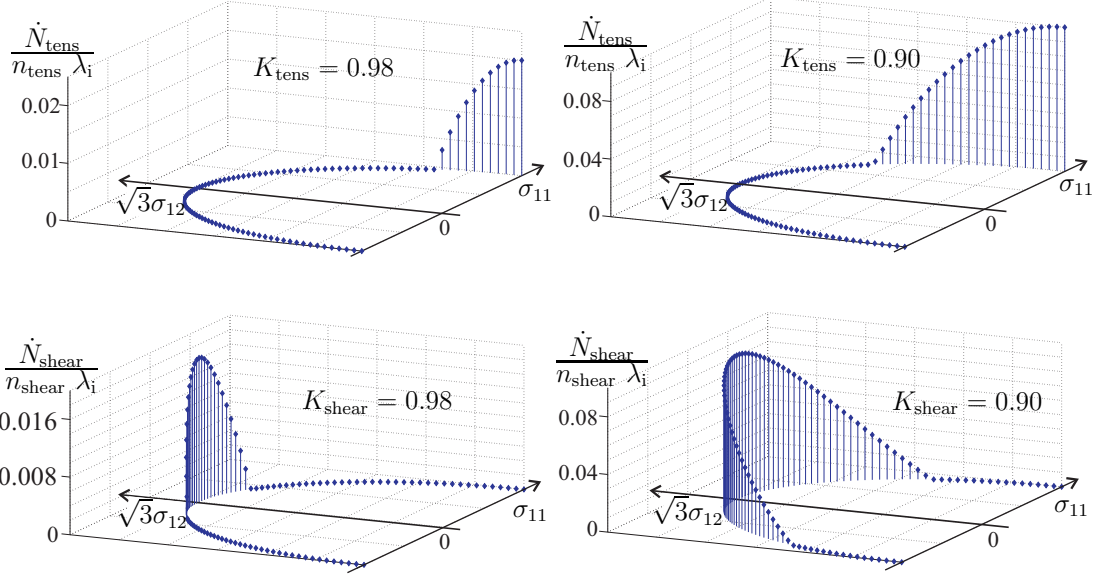


Figure 3: Distribution of void nucleation rates in the $(\sigma_{11}, \sqrt{3}\sigma_{12})$ -space where $\hat{\Sigma} = \sigma_{11}\mathbf{e}_1 \otimes \mathbf{e}_1 + \sigma_{12}(\mathbf{e}_1 \otimes \mathbf{e}_2 + \mathbf{e}_2 \otimes \mathbf{e}_1)$. Top: void nucleation rate under tension $\dot{N}_{\text{tens}}/(n_{\text{tens}} \lambda_i)$ (cf. (55)). Bottom: void nucleation rate under shear $\dot{N}_{\text{shear}}/(n_{\text{shear}} \lambda_i)$ (cf. (56)).

the effective stress space is depicted in Fig. 3 for two different values of K_{tens} . As $K_{\text{tens}} \rightarrow 1$, only the effective stress states close to uniaxial tension contribute to void nucleation. For smaller values of K_{tens} , the distribution becomes more uniform. Next, the void nucleation rate under local shear is given by

$$\dot{N}_{\text{shear}} = n_{\text{shear}} \lambda_i \left\{ \left\langle \frac{|\sigma_1 - \sigma_2|}{\sqrt{2}\mathfrak{F}} - K_{\text{shear}} \right\rangle + \left\langle \frac{|\sigma_2 - \sigma_3|}{\sqrt{2}\mathfrak{F}} - K_{\text{shear}} \right\rangle + \left\langle \frac{|\sigma_1 - \sigma_3|}{\sqrt{2}\mathfrak{F}} - K_{\text{shear}} \right\rangle \right\}. \quad (56)$$

Here, $n_{\text{shear}} \geq 0$ and $K_{\text{shear}} < 1$. Analogously to (55), the threshold K_{shear} is used to control the distribution of the nucleation rate in the stress space. As $K_{\text{shear}} \rightarrow 1$, a distinct single peak near pure shear state is observed (cf. Fig. 3). For $K_{\text{shear}} < 1$, the distribution becomes more uniform. Finally, the void nucleation rate under compression is given by

$$\dot{N}_{\text{comp}} = n_{\text{comp}} \lambda_i \langle -\text{tr}(\hat{\Sigma}) - K_{\text{comp}} \rangle, \quad (57)$$

where $n_{\text{comp}} \geq 0$ and K_{comp} are fixed material parameters. Observe that this type of void nucleation depends solely on the hydrostatic pressure $-\text{tr}(\hat{\Sigma})/3$ and the inelastic strain rate λ_i . This mechanism contributes to the overall void nucleation only if the pressure exceeds the threshold $K_{\text{comp}}/3$. Note that $\dot{N}_{\text{tens}}, \dot{N}_{\text{shear}}, \dot{N}_{\text{comp}} \geq 0$ for $n_{\text{tens}}, n_{\text{shear}}, n_{\text{comp}} \geq 0$, which forbids any void healing.

The introduced nucleation rule is compared to some classical rules in Appendix B in a qualitative way. Moreover, a concrete numerical example will be presented in Section 4.

2.7. Damage evolution equation

In this paper, for simplicity, we neglect the effects of void coalescence and suppose that the damage evolution stems solely from the void nucleation and growth

$$\dot{\Phi} = \dot{\Phi}_{\text{nucleation}} + \dot{\Phi}_{\text{growth}}. \quad (58)$$

The material expansion due to void nucleation is described by

$$\dot{\Phi}_{\text{nucleation}} = v_{\text{tens}} \dot{N}_{\text{tens}} + v_{\text{shear}} \dot{N}_{\text{shear}} + v_{\text{comp}} \dot{N}_{\text{comp}}, \quad (59)$$

where the constant parameters v_{tens} , v_{shear} , and v_{comp} stand for the characteristic void volumes. Three different parameters are used in (59) to account for the effects of different void volumes, depending on the nucleation mechanism. Next, one of the simplest expressions for the material expansion due to the dilatational void growth is given by (cf. Rice and Tracey (1969))

$$\dot{\Phi}_{\text{growth}} = d_{\text{growth}} (\Phi - \Phi_0) \lambda_i \exp\left(\sqrt{\frac{3}{2}} \frac{\text{tr} \hat{\Sigma}}{\mathfrak{F}}\right), \quad d_{\text{growth}} = \text{const} \geq 0, \quad \Phi_0 = \text{const} > 0. \quad (60)$$

Here, the parameter Φ_0 is adopted to capture the fraction of the pre-existing pores, such that the special case $\Phi = \Phi_0$ corresponds to the state without voids.

2.8. Chronological summary of the main assumptions

In Table 1 we summarize the main modeling assumptions and ideas which are utilized in the current study. Effects with geometric nonlinearities are marked by *.

Table 1: Chronological summary of the main assumptions.

Effects/phenomena	Modeling assumptions and their historical origins
Elasto-plastic kinematics *	Multiplicative decomposition (3) (Bilby et al. , 1957)
Damage-elasticity coupling	Isotropic elasticity; reduced k and μ , cf. (26) (Bristow , 1960)
Viscosity	Peryzna's overstress theory, cf. (45) (Perzyna , 1966)
Void growth	Strain-driven void growth, cf. (60) (Rice and Tracey , 1969)
Inelastic flow with damage	Normality rule for damaged material (Berg , 1969)
Elasticity *	Hyperelasticity in elastic range, cf. (28) (Simo and Ortiz , 1985)
Ductile damage	Porosity as an adequate measure of damage (Tvergaard , 1989)
Damage-induced expansion *	Multiplicative decomposition (1) (Bammann and Aifantis , 1989)
Inelastic flow *	Flow rules of Simo-Miehe type, cf. (43) (Simo and Miehe , 1992)
Nonlin. kinematic hardening *	Multiplicative decomposition (4) (Lion , 2000)
Void nucleation	New nucleation rule presented in Section 2.6

3. Numerics

3.1. Transformation of equations to the porous configuration

In order to simplify the numerical treatment of the constitutive equations, they will be transformed to the porous configuration \mathcal{K}^{por} . First, recalling (3) and (7), we note that

$$\text{tr}(\hat{\mathbf{C}}_e^n) = \text{tr}\left(\left(\mathbf{C}_{\text{ep}}^{\text{por}} \mathbf{C}_i^{\text{por}-1}\right)^n\right), \quad n = 1, 2, 3. \quad (61)$$

Analogously, using (4) and (8), we have

$$\text{tr}(\tilde{\mathbf{C}}_{\text{ie}}^n) = \text{tr}\left(\left(\mathbf{C}_i^{\text{por}} \mathbf{C}_{\text{ii}}^{\text{por}-1}\right)^n\right), \quad n = 1, 2, 3. \quad (62)$$

Therefore, due to the isotropy, the free energy (22) can be represented in the form

$$\psi = \psi_{\text{el}}(\mathbf{C}_{\text{ep}}^{\text{por}} \mathbf{C}_i^{\text{por}-1}, \Phi) + \psi_{\text{kin}}(\mathbf{C}_i^{\text{por}} \mathbf{C}_{\text{ii}}^{\text{por}-1}, \Phi) + \psi_{\text{iso}}(s_e, \Phi). \quad (63)$$

Moreover, note that for any smooth scalar-valued function α we have

$$\mathbf{A}^T \frac{\partial \alpha(\mathbf{A} \mathbf{B} \mathbf{A}^T)}{\partial (\mathbf{A} \mathbf{B} \mathbf{A}^T)} \mathbf{A} = \frac{\partial \alpha(\mathbf{A} \mathbf{B} \mathbf{A}^T)}{\partial \mathbf{B}} \Big|_{\mathbf{A}=\text{const}}. \quad (64)$$

Applying pull-back transformations to the potential relations (28)₁, (28)₂, and taking (63), (64) into account, we obtain

$$\mathbf{T}_{\text{ep}}^{\text{por}} = 2\rho_{\text{por}} \frac{\partial \psi_{\text{el}}(\mathbf{C}_{\text{ep}}^{\text{por}} \mathbf{C}_i^{\text{por}-1}, \Phi)}{\partial \mathbf{C}_{\text{ep}}^{\text{por}}} \Big|_{\mathbf{C}_i^{\text{por}}=\text{const}}, \quad \mathbf{X}^{\text{por}} = 2\rho_{\text{por}} \frac{\partial \psi_{\text{kin}}(\mathbf{C}_i^{\text{por}} \mathbf{C}_{\text{ii}}^{\text{por}-1}, \Phi)}{\partial \mathbf{C}_i^{\text{por}}} \Big|_{\mathbf{C}_{\text{ii}}^{\text{por}}=\text{const}}. \quad (65)$$

If the concrete ansatz (23), (24) is adopted, then the stresses are given by

$$\mathbf{T}_{\text{ep}}^{\text{por}} = \Phi^{-1} \left(k(\Phi) \ln \sqrt{\det(\mathbf{C}_{\text{ep}}^{\text{por}})} \mathbf{C}_{\text{ep}}^{\text{por}-1} + \mu(\Phi) \mathbf{C}_{\text{ep}}^{\text{por}-1} (\overline{\mathbf{C}_{\text{ep}}^{\text{por}} \mathbf{C}_i^{\text{por}-1}})^{\text{D}} \right). \quad (66)$$

$$\mathbf{X}^{\text{por}} = \Phi^{-1} \frac{c(\Phi)}{2} \mathbf{C}_i^{\text{por}-1} (\mathbf{C}_i^{\text{por}} \mathbf{C}_{\text{ii}}^{\text{por}-1})^{\text{D}}. \quad (67)$$

Substituting (66) into (17), for the 2nd Piola-Kirchhoff stress we obtain

$$\tilde{\mathbf{T}} = k(\Phi) (\ln \sqrt{\det(\mathbf{C})} - \ln \Phi) \mathbf{C}^{-1} + \mu(\Phi) \mathbf{C}^{-1} (\overline{\mathbf{C} \mathbf{C}_i^{\text{por}-1}})^{\text{D}}. \quad (68)$$

Next, we consider the invariants (moments) of the effective stress tensor

$$\text{tr}(\hat{\Sigma}^n) \stackrel{(21)}{=} \text{tr}((\hat{\mathbf{C}}_e \hat{\mathbf{S}}_{\text{ep}} - \hat{\mathbf{X}})^n) = \text{tr}((\mathbf{C}_{\text{ep}}^{\text{por}} \mathbf{T}_{\text{ep}}^{\text{por}} - \mathbf{C}_i^{\text{por}} \mathbf{X}^{\text{por}})^n), \quad n = 1, 2, 3. \quad (69)$$

These relations imply that the eigenvalues of $\hat{\Sigma}$ coincide with the eigenvalues of $\mathbf{C}_{\text{ep}}^{\text{por}} \mathbf{T}_{\text{ep}}^{\text{por}} - \mathbf{C}_i^{\text{por}} \mathbf{X}^{\text{por}}$. Moreover, since

$$\|\hat{\Sigma}^{\text{D}}\| = \sqrt{\text{tr}[(\hat{\Sigma}^{\text{D}})^2]}, \quad (70)$$

Table 2: Summary of the material model

$\frac{d}{dt} \mathbf{C}_i^{\text{por}} = 2 \frac{\lambda_i}{\mathfrak{F}} (\mathbf{C}_{\text{ep}}^{\text{por}} \mathbf{T}_{\text{ep}}^{\text{por}} - \mathbf{C}_i \mathbf{X})^{\text{D}} \mathbf{C}_i^{\text{por}},$	$\mathbf{C}_i _{t=0} = \mathbf{C}_i^0, \det \mathbf{C}_i^0 = 1,$
$\frac{d}{dt} \mathbf{C}_{\text{ii}}^{\text{por}} = 2 \lambda_{\text{ii}} \varkappa(\Phi) (\mathbf{C}_i \mathbf{X})^{\text{D}} \mathbf{C}_{\text{ii}}^{\text{por}},$	$\mathbf{C}_{\text{ii}} _{t=0} = \mathbf{C}_{\text{ii}}^0, \det \mathbf{C}_{\text{ii}}^0 = 1,$
$\dot{s} = \sqrt{\frac{2}{3}} \lambda_i, \quad \dot{s}_{\text{d}} = \frac{\beta(\Phi)}{\gamma(\Phi)} \dot{s} R,$	$s _{t=0} = s^0, \quad s_{\text{d}} _{t=0} = s_{\text{d}}^0,$
$\mathbf{T}_{\text{ep}}^{\text{por}} = 2 \rho_{\text{por}} \frac{\partial \psi_{\text{el}}(\mathbf{C}_{\text{ep}}^{\text{por}} \mathbf{C}_i^{-1}, \Phi)}{\partial \mathbf{C}_{\text{ep}}^{\text{por}}} \Big _{\mathbf{C}_i = \text{const}},$	$\mathbf{X} = 2 \rho_{\text{por}} \frac{\psi_{\text{kin}}(\mathbf{C}_i \mathbf{C}_{\text{ii}}^{-1}, \Phi)}{\partial \mathbf{C}_i} \Big _{\mathbf{C}_{\text{ii}} = \text{const}},$
$R = \rho_{\text{por}} \frac{\partial \psi_{\text{iso}}(s - s_{\text{d}}, \Phi)}{\partial s} \Big _{s_{\text{d}} = \text{const}},$	
$\lambda_i = \frac{1}{\eta} \left\langle \frac{f}{f_0} \right\rangle^m, \quad f = \mathfrak{F} - \sqrt{\frac{2}{3}} [K(\Phi) + R],$	$\mathfrak{F} = \sqrt{\text{tr}[(\mathbf{C} \tilde{\mathbf{T}} - \mathbf{C}_i \tilde{\mathbf{X}})^{\text{D}}]^2},$
$\dot{\Phi} = \dot{\Phi}(\hat{\mathbf{D}}_i, \hat{\Sigma}, \hat{\mathbf{X}}, \Phi), \quad \mathbf{C}_{\text{ep}}^{\text{por}} = \Phi^{-2/3} \mathbf{C},$	$\tilde{\mathbf{T}} = \Phi^{1/3} \mathbf{T}_{\text{ep}}^{\text{por}}.$

we obtain the driving force in the following form

$$\mathfrak{F} \stackrel{(54)}{=} \|\hat{\Sigma}^{\text{D}}\| = \sqrt{\text{tr}[(\mathbf{C}_{\text{ep}}^{\text{por}} \mathbf{T}_{\text{ep}}^{\text{por}} - \mathbf{C}_i \mathbf{X})^{\text{D}}]^2}. \quad (71)$$

For the hydrostatic stress, we have the transformation rule as follows

$$\text{tr}(\hat{\mathbf{C}}_e \hat{\mathbf{S}}_{\text{ep}}) = \text{tr}(\mathbf{C}_{\text{ep}}^{\text{por}} \mathbf{T}_{\text{ep}}^{\text{por}}). \quad (72)$$

Finally, in order to transform the evolution equations, we note that

$$\frac{d}{dt} \mathbf{C}_i^{\text{por}} = 2 \mathbf{F}_i^{\text{por}} \hat{\mathbf{D}}_i \mathbf{F}_i^{\text{por}}, \quad \frac{d}{dt} \mathbf{C}_{\text{ii}}^{\text{por}} = 2 \mathbf{F}_{\text{ii}}^{\text{por}} \hat{\mathbf{D}}_{\text{ii}} \mathbf{F}_{\text{ii}}^{\text{por}}. \quad (73)$$

Substituting (43) into these relations, we have

$$\frac{d}{dt} \mathbf{C}_i^{\text{por}} = 2 \frac{\lambda_i}{\mathfrak{F}} (\mathbf{C}_{\text{ep}}^{\text{por}} \mathbf{T}_{\text{ep}}^{\text{por}} - \mathbf{C}_i \mathbf{X})^{\text{D}} \mathbf{C}_i^{\text{por}}, \quad \frac{d}{dt} \mathbf{C}_{\text{ii}}^{\text{por}} = 2 \lambda_{\text{ii}} \varkappa(\Phi) (\mathbf{C}_i \mathbf{X})^{\text{D}} \mathbf{C}_{\text{ii}}^{\text{por}}. \quad (74)$$

The system of constitutive equations is summarized in Table 2.

3.2. Hybrid explicit/implicit time integration

As a preliminary step, we specify the evolution equation (74)₂ governing the backstress saturation for the case where the energy storage is described by (24). Substituting (67) into (74)₂, we obtain

$$\frac{d}{dt} \mathbf{C}_{\text{ii}}^{\text{por}} = \Phi^{-1} \lambda_{\text{ii}} \varkappa(\Phi) c(\Phi) (\mathbf{C}_i \mathbf{C}_{\text{ii}}^{-1})^{\text{D}} \mathbf{C}_{\text{ii}}^{\text{por}}. \quad (75)$$

As is typical for metal viscoplasticity, the system of underlying equations is stiff. Thus, an explicit time integration scheme would be stable only for very small time steps. In case of large $c(\Phi)$, especially severe restrictions are imposed on the time steps due to the stiff part in equation (75). In this study we benefit from the fact that this equation is similar to the evolution equation governing the Maxwell fluid (Shutov et al. , 2013). For this certain type

of Maxwell fluid, there exists an explicit update formula within the implicit time integration (Shutov et al. , 2013). Equation (75) is treated using the explicit update formula, which leads to (82). The remaining evolution equations are discretized using the explicit Euler forward method with subsequent correction of incompressibility. An obvious advantage of (82) over straightforward explicit discretization is that the solution ${}^{n+1}\mathbf{C}_{\text{ii}}^{\text{por}}$ remains bounded even for very large time steps and large values of $c(\Phi)$.¹³

Let us consider a typical time step from ${}^n t$ to ${}^{n+1} t$ with $\Delta t := {}^{n+1} t - {}^n t > 0$. Assume that ${}^{n+1}\mathbf{C} := \mathbf{C}({}^{n+1} t)$ is known. For the viscous case with $\eta > 0$, the hybrid explicit/implicit integration procedure is as follows

$$\mathbf{C}_{\text{ep}}^{\text{por}} = {}^n \Phi^{-2/3} {}^{n+1} \mathbf{C}, \quad (76)$$

$$\mathbf{T}_{\text{ep}}^{\text{por}} = {}^n \Phi^{-1} (k({}^n \Phi) \ln \sqrt{\det(\mathbf{C}_{\text{ep}}^{\text{por}})} \mathbf{C}_{\text{ep}}^{\text{por}-1} + \mu({}^n \Phi) \mathbf{C}_{\text{ep}}^{\text{por}-1} (\overline{\mathbf{C}_{\text{ep}}^{\text{por}}} \mathbf{C}_{\text{i}}^{\text{por}-1})^{\text{D}}), \quad (77)$$

$$\mathbf{X}^{\text{por}} = {}^n \Phi^{-1} \frac{c({}^n \Phi)}{2} {}^n \mathbf{C}_{\text{i}}^{\text{por}-1} ({}^n \mathbf{C}_{\text{i}}^{\text{por}} {}^n \mathbf{C}_{\text{ii}}^{\text{por}-1})^{\text{D}}, \quad R = {}^n \Phi^{-1} \gamma({}^n \Phi) ({}^n s - {}^n s_{\text{d}}), \quad (78)$$

$$\mathfrak{F} = \sqrt{\text{tr}[(\overline{(\mathbf{C}_{\text{ep}}^{\text{por}} \mathbf{T}_{\text{ep}}^{\text{por}} - {}^n \mathbf{C}_{\text{i}}^{\text{por}} \mathbf{X})^{\text{D}})^2]}, \quad f = \mathfrak{F} - \sqrt{\frac{2}{3}} [K({}^n \Phi) + R], \quad \lambda_{\text{i}} = \frac{1}{\eta} \left\langle \frac{f}{f_0} \right\rangle^m, \quad (79)$$

The inelastic flow is frozen for $\lambda_{\text{i}} = 0$:

$${}^{n+1} \mathbf{C}_{\text{i}}^{\text{por}} = {}^n \mathbf{C}_{\text{i}}^{\text{por}}, \quad {}^{n+1} \mathbf{C}_{\text{ii}}^{\text{por}} = {}^n \mathbf{C}_{\text{ii}}^{\text{por}}, \quad {}^{n+1} s = {}^n s, \quad {}^{n+1} s_{\text{d}} = {}^n s_{\text{d}}, \quad {}^{n+1} \Phi = {}^n \Phi \text{ for } \lambda_{\text{i}} = 0. \quad (80)$$

For $\lambda_{\text{i}} > 0$, the internal variables are updated in the following way:

$${}^{n+1} \mathbf{C}_{\text{i}}^{\text{por}} = \overline{{}^n \mathbf{C}_{\text{i}}^{\text{por}} + 2\Delta t \frac{\lambda_{\text{i}}}{\mathfrak{F}} (\mathbf{C}_{\text{ep}}^{\text{por}} \mathbf{T}_{\text{ep}}^{\text{por}} - {}^n \mathbf{C}_{\text{i}}^{\text{por}} \mathbf{X})^{\text{D}} {}^n \mathbf{C}_{\text{i}}^{\text{por}}}, \quad (81)$$

$${}^{n+1} \mathbf{C}_{\text{ii}}^{\text{por}} = \overline{{}^n \mathbf{C}_{\text{ii}}^{\text{por}} + \Delta t {}^n \Phi^{-1} \lambda_{\text{i}} \varkappa({}^n \Phi) c({}^n \Phi) {}^{n+1} \mathbf{C}_{\text{i}}^{\text{por}}}, \quad (82)$$

$${}^{n+1} s = {}^n s + \Delta t \sqrt{\frac{2}{3}} \lambda_{\text{i}}, \quad {}^{n+1} s_{\text{d}} = {}^n s_{\text{d}} + \Delta t \sqrt{\frac{2}{3}} \lambda_{\text{i}} \frac{\beta({}^n \Phi)}{\gamma({}^n \Phi)} R, \quad (83)$$

$$\{\sigma_1, \sigma_2, \sigma_3\} = \text{eigenvalues of } (\mathbf{C}_{\text{ep}}^{\text{por}} \mathbf{T}_{\text{ep}}^{\text{por}} - {}^n \mathbf{C}_{\text{i}}^{\text{por}} \mathbf{X}), \quad \text{tr} \hat{\Sigma} = \text{tr}(\mathbf{C}_{\text{ep}}^{\text{por}} \mathbf{T}_{\text{ep}}^{\text{por}}), \quad (84)$$

$$\dot{N}_{\text{tens}} = \dot{N}_{\text{tens}}(\lambda_{\text{i}}, \sigma_1, \sigma_2, \sigma_3, \mathfrak{F}), \quad \dot{N}_{\text{shear}} = \dot{N}_{\text{shear}}(\lambda_{\text{i}}, \sigma_1, \sigma_2, \sigma_3, \mathfrak{F}), \quad (85)$$

$$\dot{N}_{\text{comp}} = \dot{N}_{\text{comp}}(\lambda_{\text{i}}, \text{tr} \hat{\Sigma}, \mathfrak{F}), \quad (86)$$

$$\dot{\Phi}_{\text{nucleation}} = v_{\text{tens}} \dot{N}_{\text{tens}} + v_{\text{shear}} \dot{N}_{\text{shear}} + v_{\text{comp}} \dot{N}_{\text{comp}}, \quad (87)$$

$$\dot{\Phi}_{\text{growth}} = d_{\text{growth}} ({}^n \Phi - \Phi_0) \lambda_{\text{i}} \exp\left(\sqrt{\frac{3}{2}} \frac{\text{tr} \hat{\Sigma}}{\mathfrak{F}}\right), \quad \dot{\Phi} = \dot{\Phi}_{\text{nucleation}} + \dot{\Phi}_{\text{growth}}, \quad (88)$$

¹³Moreover, Silbermann et. al. (2014) have shown by a series of numerical tests that the use of the update formula (82) makes the integration procedure more robust and accurate compared to the fully explicit procedure.

$${}^{n+1}\Phi = {}^n\Phi + \Delta t \dot{\Phi}. \quad (89)$$

Note that the update formulas (81) and (82) exactly preserve the incompressibility conditions $\det \mathbf{C}_i^{\text{por}} = 1$ and $\det \mathbf{C}_{ii}^{\text{por}} = 1$ which is advantageous for the prevention of error accumulation (Shutov and Kreißig, 2010)

In case of small time steps, the hybrid explicit/implicit integration scheme (76)—(89) is more efficient than the fully implicit scheme, since the solution is given in a closed form and no iteration procedure is required. Due to the reduced computational effort, the presented algorithm is well suited for use within a globally explicit FEM procedure. The algorithm is implemented into the FEM code Abaqus/Explicit adopting the user material subroutine VUMAT. An FEM simulation of a representative boundary value problem is presented in Section 5.

4. Comparison with experiments

In order to validate the proposed material model, some experimental observations of the Bauschinger effect dependent on accumulated ductile damage are needed. In this study we use a series of quasistatic uniaxial tension-followed-by-compression and compression-followed-by-tension tests presented by Horstemeyer (1998) for a cast A356 aluminium alloy.¹⁴ The flow curves pertaining to six different experiments are shown in Figure 4 (dotted lines). As can be seen from this figure, the initial yield stress under tension coincides with the initial yield stress under compression. But, for the plastically deformed samples, the true stresses under tension are essentially smaller than the corresponding stresses under compression. We interpret this tension-compression asymmetry as a consequence of ductile damage, since the damage evolution under tension is typically more intense than under compression. For the considered cast alloy, the damage effect is significant even at low tensile strains. Moreover, a distinct Bauschinger effect is observed in all experiments (cf. Figure 4). It was noted by Jordon et al. (2007) that the Bauschinger effect induced by tensile prestrains is less pronounced than the same effect after compression.¹⁵ Such behavior indicates that the damage evolution essentially influences the kinematic hardening.

For the validation of the material model, a series of numerical tests is performed. As the reference configuration we choose the initial configuration occupied by the body at $t = 0$. Since the initial state is stress free, we put $\mathbf{C}_i^{\text{por}}|_{t=0} = \mathbf{1}$. Furthermore, the initial state of the cast material is assumed to be isotropic. Therefore, we have $\mathbf{C}_{ii}^{\text{por}}|_{t=0} = \mathbf{1}$.¹⁶ The remaining initial conditions are given by $s|_{t=0} = s_d|_{t=0} = 0$, $\Phi|_{t=0} = 1$.

We define the set of material parameters as follows. Firstly, void growth is neglected here: $d_{\text{growth}} = 0$.¹⁷ Moreover, we neglect void nucleation under compression by putting $n_{\text{comp}} = 0$. Thus, the values of K_{comp} and v_{comp} become irrelevant. The elasticity parameters k_0 and μ_0 are

¹⁴Although the ductility of this alloy is very limited, it plays an important role in the automotive industry. Its microstructural characterization was presented by Gall et al. (1999).

¹⁵The same asymmetry of Bauschinger effect was also observed in porous sintered steels by Deng et al. (2005).

¹⁶Constitutive relations can be adopted to the initial plastic anisotropy by an appropriate choice of the initial conditions (Shutov et al., 2012).

¹⁷Thus, we assume for simplicity that the damage in this case is dominated by void nucleation.

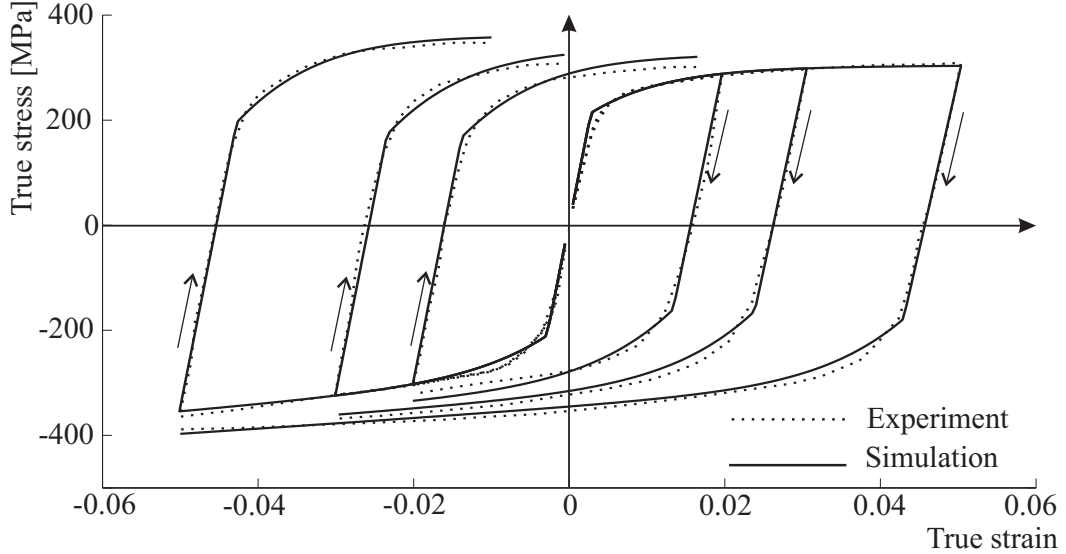


Figure 4: Uniaxial tension-followed-by-compression and compression-followed-by-tension tests. Experimental data for the cast A356 aluminium alloy (Horstemeyer , 1998) are shown by dotted lines. Simulation results are depicted by solid lines.

identified using the stress-strain curve in the elastic range. The initial yield stress K_0 is estimated at a transition from elasticity to plasticity under quasistatic loading conditions. In general, the viscosity parameters m and η can be estimated using a series of tests with different loading rates. In this section we neglect the real viscous effects and adopt the parameters m and η only as numerical regularization parameters. All simulations will be performed with a low loading rate such that the overstress f will remain below 10 MPa. Next, the nucleation parameters K_{tens} , K_{shear} , n_{tens} , and n_{shear} should be identified by counting the void nucleation sites as a function of strain under different loading conditions (Horstemeyer et al. , 2000). In this section, v_{tens} and v_{shear} are roughly estimated by assuming that each void has a volume of approximately 10^{-7}mm^3 . In general, the parameters v_{tens} and v_{shear} should be identified by measuring the volume changes induced by ductile damage. Finally, the remaining parameters can be reliably identified using the experimental flow curves shown in Figure 4. Note that only 7 material parameters (K_0 , γ_0 , β_0 , α_0 , c_0 , IRR, KRR) were adjusted to fit the flow curves. The set of material parameters which is used to describe the material response is summarized in Table 3.

The stress response of the material can be described by the proposed material model with sufficient accuracy (cf. Figure 4). Within the numerical simulation, the real Bauschinger effect is slightly underestimated, which leads to a minor discrepancy between the simulated and the real stress responses shortly after the secondary yielding. Following the ideas of Chaboche (1989), this discrepancy can be reduced by introducing additional backstress.¹⁸

During the phase of 5% prestrain under tension (within the tension-followed-by-compression test), the theoretical value of Φ can be up to $\Phi_{0.05} = 1.00428$. The elastic modulus $E_{0.05}$ following

¹⁸For a model of multiplicative type it was carried out by Shutov et al. (2010).

Table 3: Material parameters.

parameter	value	brief explanation
k_0	73500 MPa	initial bulk modulus
μ_0	28200 MPa	initial shear modulus
c_0	6399.8 MPa	kinematic hardening parameter
\varkappa_0	$0.015106 \text{ MPa}^{-1}$	kinematic hardening parameter
γ_0	1442.2 MPa	isotropic hardening parameter
β_0	1.852	isotropic hardening parameter
K_0	210 MPa	initial yield stress
m	1	viscosity parameter
η	100 s	viscosity parameter
KRR	67.63	kinematic hardening reduction rate
IRR	29.97	isotropic hardening reduction rate
BRR	45	bulk modulus reduction rate
SRR	30	shear modulus reduction rate
v_{tens}	10^{-7} mm^3	void volume nucleated under tension
v_{shear}	10^{-7} mm^3	void volume nucleated under shear
n_{tens}	$2773000 \text{ mm}^{-3} \text{MPa}^{-1}$	void nucleation parameter (tension)
K_{tens}	0.79	void nucleation parameter (tension)
n_{shear}	$17188000 \text{ mm}^{-3} \text{MPa}^{-1}$	void nucleation parameter (shear)
K_{shear}	0.9353	void nucleation parameter (shear)
n_{comp}	$0 \text{ mm}^{-3} \text{MPa}^{-1}$	void nucleation parameter (compression)
f_0	1 MPa	constant (not a material parameter)

5% tension and the initial modulus E_0 are computed with

$$E_{0.05} = \frac{9k(\Phi_{0.05}) \mu(\Phi_{0.05})}{3k(\Phi_{0.05}) + \mu(\Phi_{0.05})}, \quad E_0 = \frac{9k_0 \mu_0}{3k_0 + \mu_0}. \quad (90)$$

The numerical simulation yields $E_{0.05} = 0.8729 E_0$, which corresponds to 12.7% reduction. At the same time, the elastic modulus is unaffected by the 5% compression. As can be seen from Figure 4, the elastic unloading is captured by the model with ample accuracy, both for tensional and compressional prestrains.

Another noteworthy aspect is the following. According to Table 3, $\text{KRR} \approx 2 \text{ IRR}$. This means that the deterioration of the kinematic hardening progresses twice as fast as the deterioration of the isotropic hardening. Thus, the concept of effective stresses combined with the strain equivalence principle is too restrictive for the cast A356 aluminium alloy, since this concept implies that the kinematic and isotropic hardening deteriorate with the same rate (Grammenoudis et al. , 2009; Bröcker and Matzenmiller , 2014).

Uniaxial experiments are insufficient to validate the void nucleation rule proposed in the current study. Such a validation should be based on experimental observation of void nucleation for different loading conditions. In this study we use experimental data previously reported by

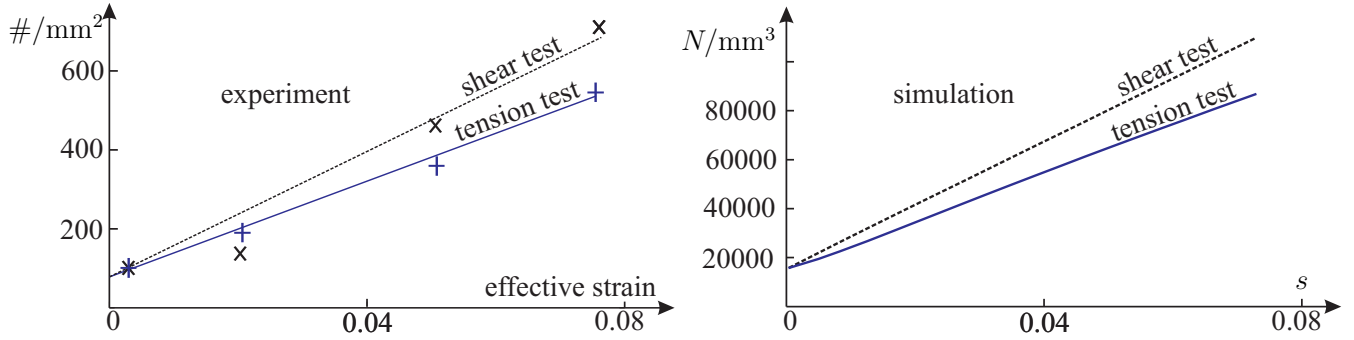


Figure 5: Left: Experimental results for the void nucleation in the cast A356 aluminium alloy (Horstemeyer et al. , 2000). Number of voids per unit area is depicted. Right: Simulation results for the void number N as a function of the accumulated inelastic arc-length s . Depending on the choice of the material parameters, the void nucleation rate under shear may exceed the nucleation rate under tension.

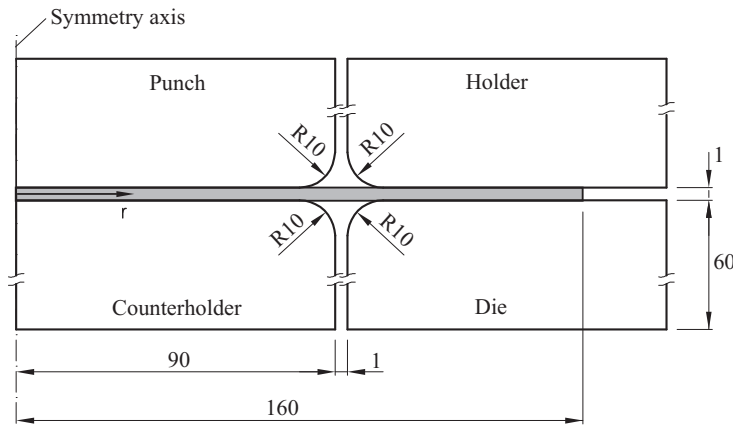


Figure 6: Setup of the axisymmetric deep drawing.

Horstemeyer et al. (2000) for the cast A356 aluminium alloy, see Figure 5 (left). Tension and torsion are considered here. The simulated void number N is plotted versus the accumulated inelastic arc-length s in Figure 5 (right). For the simulation of both tests, the initial value of 15000 voids per mm^3 is adopted. The simulation results correspond qualitatively to the experimental data.

5. FEM solution of a representative boundary value problem

An axisymmetric deep drawing of a circular sheet metal blank is considered in this section to demonstrate the applicability of the new model and to test the stability of the implemented numerical procedures. The setup is depicted in Fig. 6. The overall forming process consists of three steps:

- 1 Preliminary step: Forces are gradually applied both to holder and counterholder.
- 2 Deep drawing: The punch pushes the blank into the die.



Figure 7: Deformed state after deep drawing. Only a quarter of the blanket is shown.

3 Spring back: The blank is released from any contact.

The material of the blank is described by the proposed material model with parameters taken from Table 3, which correspond to the A356 aluminium alloy.¹⁹ The remaining bodies are assumed to be rigid. Coulomb friction is assumed with a friction coefficient of 0.1. A quasistatic loading rate is chosen such that the kinetic energy is negligible compared to the work of external forces. Mass scaling, which is typically adopted to speed up computation, is not used here. The FE mesh consists of 1950 elements of ABAQUS type CAX4R (4-node bilinear axisymmetric quadrilateral element with reduced integration, hourglass control, linear geometric order). Steps 1, 2 and 3 last 0.01s, 0.10s and 0.12s, respectively. The simulation required 460 563, 4 638 783 and 5 592 654 increments for steps 1, 2 and 3, respectively.

It is known that the deterioration of elastic properties and the Bauschinger effect have a strong impact on the spring back (Wagoner et al. , 2013). The deformed state after deep drawing is shown in Fig. 7.²⁰ Fig. 8 shows the distribution of the von Mises equivalent stress after deep drawing and after the spring back. Fig. 9 provides the distribution of the maximum and minimum principal stresses after the spring back. Note that the residual stresses remain high compared to the initial yield stress ($K_0 = 210$ MPa). By comparison with the resulting inelastic arc length field s (cf. Fig. 10 (left)), it becomes clear that highest residual stresses appear in regions with a considerable gradient of s . The distribution of the damage measure $\Phi - 1$ after spring back is depicted in Fig. 10 (right). Note that $\Phi - 1$ remains in the range of a few percent and the damage is concentrated in the deep-drawn section. The observed damage hot spots are considered as a precursor of failure.

Note that a generic local approach to ductile damage is adopted in this study. In general, the simulation results for local damage models are pathologically mesh-dependent in case of localizing deformation processes. Thus, the presented model should not be used for the analysis of post-localization structural behavior. The post-localization analysis should be based on nonlocal

¹⁹ Note that the formability of cast alloys is low. For that reason, the deep drawing process simulated here will be hardly implemented in practice. Instead, wrought alloys are used. Nevertheless, we consider this cast alloy here as an example material because of a rich literature dealing with its experimental characterization. The simulation results of this subsection are used to validate the robustness and accuracy of the numerical algorithm and to demonstrate the practicability of our approach.

²⁰An animated version of the FEM solution can be found under <http://youtu.be/YhEwI0cpIGQ> and <http://youtu.be/r6rY2oRUNqQ>.

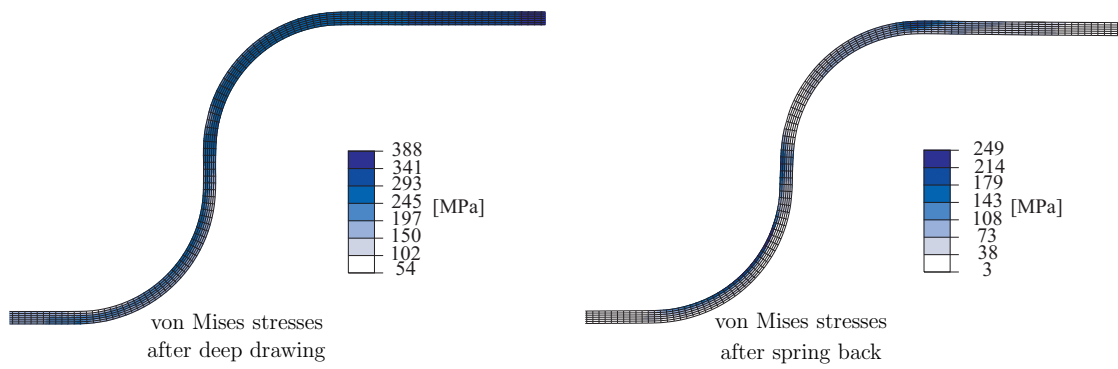


Figure 8: Distribution of von Mises stresses after deep drawing (left) and after spring back (right).

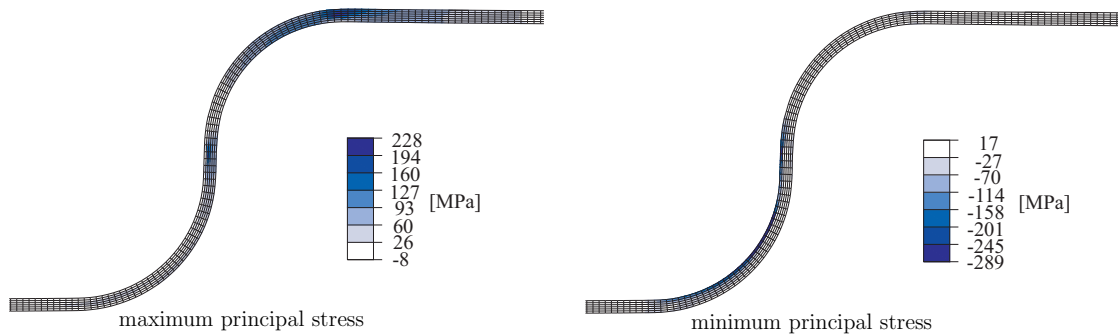


Figure 9: Distribution of maximum and minimum principal stresses after the spring back.

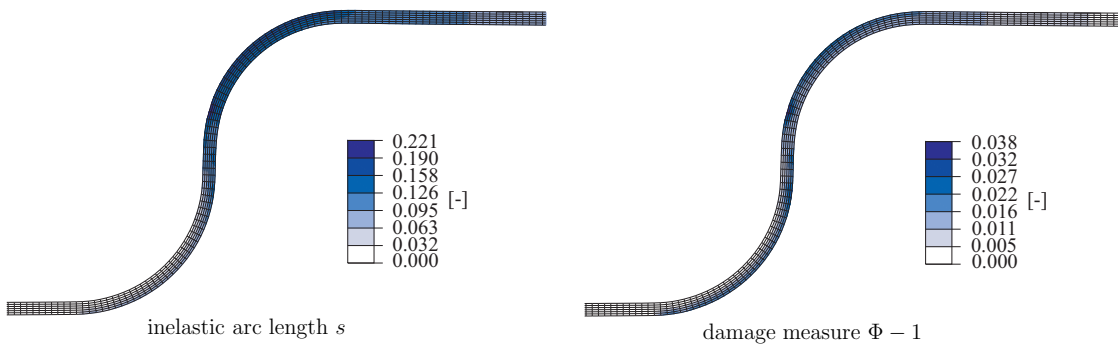


Figure 10: Distribution of the inelastic arc length s (left) and damage measure $\Phi - 1$ (right) after the spring back.

damage models which enrich the continuum formulation by introducing a physics-based length scale (see Bažant and Jirásek (2002); Anand et al. (2012); Ahad et al. (2014); Nguyen et al. (2015) and references therein). Some sort of regularization is also possible using the viscosity, which is available in the current model. Unfortunately, this technique is effective only in a narrow range of deformation rates (Bažant and Jirásek, 2002). Still, the proposed local material model is useful for estimating the process parameters which lead to undesired strain localization. No strain localization was observed in the current simulation.

6. Discussion and conclusion

A *thermodynamically consistent* approach to ductile damage and nonlinear kinematic hardening is suggested within the framework of multiplicative plasticity. It is well established that at the early stage of the damage process the damage is adequately described by the scalar porosity variable (see, for example, Tvergaard (1989)). Thus, for simplicity, isotropic damage with no prominent orientation is assumed in this study. To extend the current model to the case of anisotropic damage, some physics-based tensorial damage quantities can be introduced.²¹

The damage-induced *volume change* is taken into account explicitly by the model kinematics for the accurate prediction of the hydrostatic stress component. Another feature of the proposed model is that isotropic and kinematic hardening *deteriorate differently* for increasing damage, which is essential for an accurate description of the real material response. Moreover, the *deterioration of elastic properties* is introduced for the correct prediction of residual stresses and spring back. Next, a *refined void nucleation rule* is constructed in this study aiming at accurate description of the complex behavior of porous ductile metals with second phases. In particular, the new rule is suitable for materials which exhibit a higher void nucleation rate under torsion than in case of tension. The proposed model is validated using the experimental observations of the void nucleation under various loading conditions and experimental stress-strain curves. These curves carry information on the evolution of plastic anisotropy, reduction of strain hardening capacity, and deterioration of elastic properties.

The phenomenological formulation can be enriched by physics-based rules for void nucleation, growth and coalescence. The restrictions imposed on these relations by the Clausius-Duhem inequality are *obtained in an explicit form*. Interestingly, a cut-off value for hydrostatic pressure is obtained from irreversible thermodynamics in a natural way (cf. (52)₂).

A relatively large number of material parameters is introduced due to a variety of nonlinear phenomena covered by the model. In some applications, however, certain parts of the model can be switched off to reduce the number of parameters. For instance, some elementary or classical void nucleation rules can be adopted (cf. Appendix A). Alternatively, the nucleation rules (55) – (57) can be calibrated using experiments (cf. Su et al. (2010)) or lower-scale models (cf. Gall et al. (2000); Dandekar and Shin (2011)).

²¹Different approaches to anisotropic damage can be found in Murakami and Ohno (1980); Kachanov (1986); Chaboche (1993); Krajcinovic (1996); Brünig (2001, 2003); Zapara et al. (2010, 2012); Voyiadjis et al. (2012); Tutyshkin et al. (2014).

An efficient hybrid explicit/implicit numerical procedure is presented. This procedure exhibits *increased stability and accuracy* being compared to a purely explicit time stepping. The feasibility of the proposed algorithm is tested numerically and the algorithm is shown to be suitable for explicit FEM analysis.

Although the model has been developed for forming simulations, another promising application includes the prediction of damage and plastic anisotropy in ultra-fine grained materials produced by severe plastic deformations (Wagner et al. , 2010; Frint et al. , 2011; Neugebauer et al. , 2012). An extension of the framework to models of creep damage mechanics (Altenbach et al. , 2002; Altenbach , 2003) is possible as well.

Acknowledgement

The financial support provided by DFG within SFB 692 is acknowledged.

Appendix A (some void nucleation rules)

In this appendix we briefly recall some of the void nucleation rules that are available in the literature. For simplicity, only monotonic loading is considered here. Let N be the void number per unit volume of the reference configuration. A very simple void nucleation rule says that N is a linear function of the accumulated plastic arc-length s (Gurland , 1972)

$$\dot{N} = \lambda_i n_{\text{Gurland}} \stackrel{(44)}{\Rightarrow} \frac{\partial N}{\partial s} = \sqrt{3/2} n_{\text{Gurland}}. \quad (91)$$

Here, $n_{\text{Gurland}} \geq 0$ is a material parameter. In other words, the void nucleation rate $\frac{\partial N}{\partial s}$ is assumed to be independent of the stage of the deformation process and of the stress state.

In order to capture the dependence on the stage of the deformation process, relation (91) was generalized by Gurson (1977). Here we consider a popular modification of Gurson's rule. Let f_{void} be the void volume fraction. For the strain-controlled nucleation, Chu and Needleman (1980) assumed that the void nucleation is governed by a normal distribution law

$$\dot{f}_{\text{void}} = \frac{f_N}{S_N \sqrt{2\pi}} \exp \left[-\frac{1}{2} \left(\frac{s - s_N}{S_N} \right)^2 \right] \dot{s}, \quad (92)$$

where $f_N, S_N, s_N \geq 0$ are material parameters; s denotes the accumulated plastic arc-length. Note that (91) can be approximated by (92) with large f_N and S_N and by assuming that \dot{f}_{void} is proportional to \dot{N} . Another modification of Gurson's rule was proposed by Chu and Needleman (1980) for stress-controlled nucleation.

Rule (92) is sufficiently accurate for some alloys (Chen and Worswick , 2008). However, in ductile metals with second phases, a complex dependence of void nucleation on the stress state can be observed. For instance, torsion induces a higher void nucleation rate than tension in the cast A356 aluminum (Horstemeyer et al. , 2000). In order to account for this effect, the following void nucleation rule was proposed by Horstemeyer and Gokhale (1999). First, recall

that $\hat{\Sigma}$ is the effective stress tensor. Let J_2 and J_3 be the invariants of the deviatoric part $\hat{\Sigma}^D$. The hydrostatic stress component is captured by $\text{tr}\hat{\Sigma}$. The void nucleation is governed by

$$\dot{N} = \lambda_i N \left[p_1 \left(\frac{4}{27} - \frac{J_3^2}{J_2^3} \right) + p_2 \frac{J_3}{J_2^{3/2}} + p_3 \frac{|\text{tr}\hat{\Sigma}|}{J_2^{1/2}} \right], \quad (93)$$

where p_1 , p_2 and p_3 are material parameters.

Appendix B (discussion of void nucleation rules)

Let us compare the void nucleation rules presented in Appendix A with the new rule introduced in Section 2.6. This comparison is based on different criteria, such as the saturation of the void number under monotonic loading, the role played by the hydrostatic stress component, and the increased nucleation rate under torsion compared to tension.

Saturation: It is usually assumed that the voids nucleate at certain inclusions, or, more generally, at second phases which are sites of local stress raisers. Thus, the total number of voids is limited by the number of inclusions of a certain type. Gurland's rule (cf. (91)) predicts a linear accumulation of voids, without any saturation. A nearly linear void accumulation is also predicted by the newly constructed relations (53) – (57) (cf. Figure 5). If needed, the saturation can be introduced by a simple modification, which is not considered in the current study. Next, the rule from Chu and Needleman (cf. (92)) is realistic in the sense that the maximum void volume fraction is bounded due to the saturation of the void nucleation. Finally, the rule from Horstemeyer and Gokhale (cf. (93)) predicts even an *accelerated* void nucleation. More precisely, the void number under monotonic loading increases exponentially. Interestingly, the rule from Horstemeyer and Gokhale says that no voids can be created in initially void-free material. Indeed, if $N|_{t=0} = 0$ then (93) yields $N \equiv 0$.

The role of hydrostatic stress: The influence of the hydrostatic stress component is neglected by both (91) and (92). In contrast to this, the new nucleation rule (55) is highly sensitive to $\text{tr}\hat{\Sigma}$ such that for larger hydrostatic stresses increased nucleation rates are predicted. Interestingly, the rule from Horstemeyer and Gokhale (cf. (93)) operates with the absolute value of the hydrostatic stress component $|\text{tr}\hat{\Sigma}|$. Thus, the sign of $\text{tr}\hat{\Sigma}$ is irrelevant!

Increased nucleation rate under torsion: As already mentioned above, torsion may induce a higher void nucleation rate than tension. The classic rules from Gurland as well as Chu

Table 4: Qualitative analysis of the void nucleation rules.

Nucleation rule	Equation	Asymptotic behavior	Role of hydrostatic stress	Increased nucl. rate under torsion
Gurland (1972)	(91)	linear growth	irrelevant	impossible
Chu and Needleman (1980)	(92)	saturation	irrelevant	impossible
Horstemeyer and Gokhale (1999)	(93)	exponential growth	sign of hydrostatic stress is irrelevant	possible
New rule (current study)	(53) – (57)	linear growth	sensitive to hydrostatic stress	possible

and Needleman cannot describe this effect. By appropriate choice of material parameters, the rule from Horstemeyer and Gokhale and the new rule introduced in Section 2.6 are capable of reproducing this type of behavior. Note that different systems of invariants are used in these rules.

The theoretical results are summarized in Table 4. In conclusion, note that the assumption of linear growth of the void number is compatible with the experimental data available for the cast A356 aluminium (see Figure 5).

References

- Ahad, F.R., Enakoutsa, K., Solanki, K.N., Bammann, D.J., 2014. Nonlocal modeling in high-velocity impact failure of 6061-T6 aluminum. *International Journal of Plasticity* 55, 108–132.
- Altenbach, H., Huang, C., Naumenko, K., 2002. Creep-damage predictions in thin-walled structures by use of isotropic and anisotropic damage models. *Journal of Strain Analysis for Engineering Design* 37(3), 265–275.
- Altenbach, H., 2003. Topical problems and applications of creep theory. *International Applied Mechanics* 39(6), 631–655.
- Anand, L., Aslan, O., Chester, S.A., 2012. A large-deformation gradient theory for elastic-plastic materials: Strain softening and regularization of shear bands. *International Journal of Plasticity* 30–31, 116–143.
- Bammann, D.J., Aifantis, E.C., 1989. A damage model for ductile metals. *Nucl. Eng. Design* 116, 355–362
- Bammann, D.J., Solanki, K.N., 2010. On kinematic, thermodynamic, and kinetic coupling of a damage theory for polycrystalline material. *International Journal of Plasticity* 26, 775–793.
- Bao, Y., Wierzbicki, T., 2005. On the cut-off value of negative triaxiality for fracture. *Engineering Fracture Mechanics* 72, 1049–1069.
- Barlat, F., Ferreira Duarte, J.M., Gracio, J.J., Lopes, A.B., Rauch, E.F., 2003. Plastic flow for non-monotonic loading conditions of an aluminum alloy sheet sample. *International Journal of Plasticity* 19, 1215–1244.
- Barlat, F., Gracio, J.J., Lee, M.-G., Rauch, E.F., Vincze, G., 2011. An alternative to kinematic hardening in classical plasticity. *International Journal of Plasticity* 27, 1309–1327.
- Bažant, Z.P., Jirásek, M., 2002. Nonlocal Integral Formulations of Plasticity and Damage: Survey of Progress. *Journal of Engineering Mechanics* 128, 1119–1149.
- Berg C.A., 1969. Plastic dilation and void interaction. In: Proc of the Batelle Memorial Institute symposium on inelastic processes in solids, 171–209.
- Besson, J., 2010. Continuum models of ductile fracture: a review. *Int. J. Damage Mech.* 19, 3–52.

- Bilby, B.A., Gardner, L.R.T., Stroh, A.N., 1957. Continuous distributions of dislocations and the theory of plasticity. Proceedings of the 9th International Congress of Applied Mechanics, vol. 8. University de Bruxelles, Brussels, 35–44.
- Brepols, T., Vladimirov, I. N., Reese, S., 2013. Comparison of hyper- and hypoelastic-based formulations of elastoplasticity with applications to metal forming. *Key Engineering Materials* 554-557, 2321–2329.
- Brepols, T., Vladimirov, I. N., Reese, S., 2014. Numerical comparison of isotropic hypo- and hyperelastic-based plasticity models with application to industrial forming processes. *International Journal of Plasticity* 63, 18–48.
- Bristow, J. R., 1960. Microcracks, and the static and dynamic elastic constants of annealed and heavily cold-worked metals. *British Journal of Applied Physics* 11, 81–85.
- Bröcker, C., Matzenmiller, A., 2013. An enhanced concept of rheological models to represent nonlinear thermoviscoplasticity and its energy storage behavior. *Continuum Mechanics and Thermodynamics* 25(6), 749–778
- Bröcker, C., Matzenmiller, A., 2014. On the generalization of uniaxial thermoviscoplasticity with damage to finite deformations based on enhanced rheological models. *Technische Mechanik* 34, 142–165.
- Brünig, M., 2001. A framework for large strain elasticplastic damage mechanics based on metric transformations. *Int. J. Eng. Sci.* 39, 1033–1056.
- Brünig, M., 2003. An anisotropic ductile damage model based on irreversible thermodynamics. *International Journal of Plasticity* 19, 1679–1713.
- Brünig, M., Gerke, S., Hagenbrock, V., 2014. Stress-state-dependence of damage strain rate tensors caused by growth and coalescence of micro-defects. *International Journal of Plasticity* 63, 49–63.
- Canadija, M., Brnic, J., 2004. Associative coupled thermoplasticity at finite strain with temperature-dependent material parameters. *International Journal of Plasticity* 20, 1851–1874.
- Canadija, M., Mosler, J., 2011. On the thermomechanical coupling in finite strain plasticity theory with non-linear kinematic hardening by means of incremental energy minimization. *International Journal of Solids and Structures* 48, 1120–1129.
- Chaboche, J. L., 1989. Constitutive equations for cyclic plasticity and cyclic viscoplasticity. *International Journal of Plasticity* 5, 247–302.
- Chaboche, J.L., 1993. Development of continuum damage mechanics for elastic solids sustaining anisotropic and unilateral damage. *Int. J. Damage Mech.* 2, 311–329.
- Chen, Z., Worswick, M.J., 2008. Investigation of void nucleation in Al-Mg sheet. *Materials Science and Engineering A* 483–484, 99–101.

- Chu, C.C., Needleman, A. 1980. Void nucleation effects in biaxially stretched sheets. *Journal of Engineering Materials and Technology* 102 (3), 249–256.
- Clayton, J.D., Hartley, C.S., McDowell, D.L., 2014. The missing term in the decomposition of finite deformation. *International Journal of Plasticity* 52, 51–76.
- Dandekar, C.R., Shin, Y.C., 2011. Molecular dynamics based cohesive zone law for describing Al–SiC interface mechanics. *Composites: Part A* 42, 355–363.
- Deng, X., Piotrowski, G.B., Williams, J.J., Chawla, N., 2005. Effect of porosity and tension-compression asymmetry on the Bauschinger effect in porous sintered steels. *International Journal of Fatigue* 27, 1233–1243.
- Dettmer, W., Reese, S., 2004. On the theoretical and numerical modelling of Armstrong-Frederick kinematic hardening in the finite strain regime. *Comput. Methods Appl. Mech. Eng.* 193, 87–116.
- Frint, P., Hockauf, M., Halle, T., Strehl, G., Lampke, T., Wagner, M.F.-X., 2011. Microstructural features and mechanical properties after industrial scale ECAP of an Al–6060 alloy. *Materials Science Forum* 667-669, 1153–1158.
- Fritzen, F., Forest, S., Böhlke, T., Kondo D., Kanit, T., 2012. Computational homogenization of elasto-plastic porous metals. *International Journal of Plasticity* 29, 102–119.
- Gall, K.A., Yang, N., Horstemeyer, M.F., McDowell, D.L., Fan, J., 1999. The Debonding and fracture of Si particles during the Fatigue of a cast AlSi alloy. *Metall. Trans. A* 30, 3079–3088.
- Gall, K., Horstemeyer, M.F., Schilfgaard, M. V., Baskes, M.I., 2000. Atomistic simulations on the tensile debonding of an aluminum-silicon interface. *Journal of the Mechanics and Physics of Solids* 48, 2183–2212.
- Goods, S.H., Brown, L.M., 1979. The nucleation of cavities by plastic deformation. *Acta Metallurgica* 27, 1–15.
- Grammenoudis, P., Tsakmakis, Ch., Hofer, D., 2009. Micromorphic continuum. Part II. Finite deformation plasticity coupled with damage. *International Journal of Non-Linear Mechanics* 44, 957–974.
- Gurland, J., 1972. Observations on the fracture of cementite particles in a spheroidized 1.05% C steel deformed at room temperature. *Acta Metallurgica* 20(5), 735–741.
- Gurson, A.L., 1977. Continuum theory of ductile rupture by void nucleation and growth: Part I Yield criteria and flow rules for porous ductile media. *Journal of Engineering Materials and Techniques* 99(1), 2–15.
- Hammi, Y., Horstemeyer, M.F., 2007. A physically motivated anisotropic tensorial representation of damage with separate functions for void nucleation, growth, and coalescence. *International Journal of Plasticity* 23, 1641–1678.

- Hartmann, S., Quint, K.J., Arnold, M., 2008. On plastic incompressibility within time-adaptive finite elements combined with projection techniques. *Computer Methods in Applied Mechanics and Engineering* 198, 173–178.
- Hashiguchi, K., Yamakawa, Y., 2012. *Introduction to Finite Strain Theory for Continuum Elastoplasticity*, John Wiley & Sons.
- Haupt, P., 2002. *Continuum Mechanics and Theory of Materials*, 2nd edition, Springer.
- Helm, D., 2001. *Formgedächtnislegierungen, experimentelle Untersuchung, phänomenologische Modellierung und numerische Simulation der thermomechanischen Materialeigenschaften*, PhD Thesis (Universitätsbibliothek Kassel).
- Henann, D.L., Anand, L., 2009. A large deformation theory for rate-dependent elasticplastic materials with combined isotropic and kinematic hardening. *International Journal of Plasticity* 25, 1833–1878.
- Horstemeyer, M. F., 1998. Damage influence on Bauschinger effect of a cast A356 aluminium alloy. *Scripta Materialia* 39(11), 1491–1495.
- Horstemeyer, M.F., Gokhale, A.M., 1999. A void crack nucleation model for ductile metals. *International Journal of Solids and Structures* 36, 5029–5055.
- Horstemeyer, M. F., Lathrop, J., Gokhale, A. M., Dighe, M., 2000. Modeling stress state dependent damage evolution in a cast Al-Si-Mg aluminum alloy, *Theoretical and Applied Fracture Mechanics* 33, 31–47.
- Johansson, G., Ekh, M., Runesson, K., 2005. Computational modeling of inelastic large ratcheting strains. *International Journal of Plasticity* 21, 955–980.
- Jordon, J.B., Horstemeyer, M.F., Solanki, K., Xue, Y., 2007. Damage and stress state influence on the Bauschinger effect in aluminum alloys. *Mechanics of Materials* 39, 920–931.
- Kachanov, L.M., 1986. *Introduction to Continuum Damage Mechanics*. Kluwer, Dordrecht.
- Khan, A.S., Huang, S., 1995. *Continuum Theory of Plasticity*, John Wiley & Sons.
- Khan, A.S., Liu, H., 2012. Strain rate and temperature dependent fracture criteria for isotropic and anisotropic metals. *International Journal of Plasticity* 37, 1–15.
- Krajcinovic, D., 1996. *Damage Mechanics*. Elsevier Science BV, Amsterdam.
- Krawietz, A., 1986. *Materialtheorie: Mathematische Beschreibung des phänomenologischen thermomechanischen Verhaltens*. Springer Berlin Heidelberg.
- Lin, R.C., Brocks, W., 2006. On a finite-strain viscoplastic law coupled with anisotropic damage: theoretical formulations and numerical applications. *Arch. Appl. Mech.* 75, 315–325.

- Lion, A., 2000. Constitutive modelling in finite thermoviscoplasticity: a physical approach based on nonlinear rheological elements, *International Journal of Plasticity* 16, 469–494.
- McAuliffe, C., Waisman, H., 2015. A unified model for metal failure capturing shear banding and fracture. *International Journal of Plasticity* 65, 131–151.
- Marini, B., Mudry, F., Pineau, A., 1985. Experimental study of cavity growth in ductile rupture. *Engineering Fracture Mechanics* 6, 989–996.
- Menzel, A., Ekh, M., Runesson, K., Steinmann, P., 2005. A framework for multiplicative elasto-plasticity with kinematic hardening coupled to anisotropic damage. *International Journal of Plasticity* 21, 397–434.
- Murakami, S., Ohno, N.A., 1980. Continuum theory of creep and creep damage. In: Ponter, A.R.S., Hayhurst, D.R. (eds.) *Creep in Structures*. Springer, Berlin, 422–443.
- Neugebauer, R., Sterzing, A., Selbmann, R., Zachäus, R., Bergmann, M., 2012. Gradation extrusion - Severe plastic deformation with defined gradient. *Materials Science and Engineering Technology* 43(7), 582–588.
- Nguyen, G. D., Korsunsky, A. M., Belnoue, J. P.-H., 2015. A nonlocal coupled damage-plasticity model for the analysis of ductile failure. *International Journal of Plasticity* 64, 56–75.
- Palmov, V., 1998. *Vibrations of Elasto-Plastic Bodies*. In: *Foundations of Engineering Mechanics*. Springer.
- Palmov, V.A., 2008. Constitutive equations of thermoelastic, thermoviscous and thermoplastic materials. Politechnic University Publishing House, St. Petersburg. (In Russian)
- Pardoen, T., Hutchinson, J.W., 2000. An extended model for void growth and coalescence. *Journal of the Mechanics and Physics of Solids* 48, 2467–2512.
- Perzyna, P., 1966. Fundamental problems in visco-plasticity, in: G. Kuerti (Ed.), *Advances in Applied Mechanics*, vol. 9, Academic Press, New York, 243–377.
- Rabotnov, Yu.N., 1969. *Creep Problems in Structural Members*. Amsterdam, North-Holland.
- Reiner, M. *Deformation, Strain and Flow. An Elementary Introduction to Rheology*. London, 2nd edition (H.K. Lewis).
- Rice, J.R., Tracey, D.M., 1969. On the ductile enlargement of voids in triaxial stress fields. *Journal of the Mechanics and Physics of Solids* 17, 201–217.
- Rousselier, G., 1987. Ductile fracture models and their potential in local approach of fracture. *Nuclear Engineering and Design* 105, 97–111.
- Shutov, A.V., Kreißig, R., 2008a. Finite strain viscoplasticity with nonlinear kinematic hardening: Phenomenological modeling and time integration. *Computer Methods in Applied Mechanics and Engineering* 197, 2015–2029.

- Shutov, A.V., Kreißig, R., 2008b. Application of a coordinate-free tensor formalism to the numerical implementation of a material model. *ZAMM* 88(11), 888–909.
- Shutov, A. V., Kreißig, R., 2010. Geometric integrators for multiplicative viscoplasticity: analysis of error accumulation. *Computer Methods in Applied Mechanics and Engineering* 199, 700–711.
- Shutov, A.V., Panhans, S., Kreißig, R., 2011. A phenomenological model of finite strain viscoplasticity with distortional hardening. *ZAMM* 91(8), 653–680.
- Shutov, A.V., Ihlemann, J., 2011. On the simulation of plastic forming under consideration of thermal effects. *Materials Science and Engineering Technology* 42(7), 632–638.
- Shutov, A.V., Kuprin, C., Ihlemann, J., Wagner, M.F.-X., Silbermann, C., 2010. Experimentelle Untersuchung und numerische Simulation des inkrementellen Umformverhaltens von Stahl 42CrMo4, *Materialwissenschaft und Werkstofftechnik* 41(9), 765–775.
- Shutov, A.V., Pfeiffer, S., Ihlemann, J., 2012. On the simulation of multi-stage forming processes: invariance under change of the reference configuration. *Materials Science and Engineering Technology* 43(7), 617–625.
- Shutov, A.V., Landgraf, R., Ihlemann, J., 2013. An explicit solution for implicit time stepping in multiplicative finite strain viscoelasticity. *Computer Methods in Applied Mechanics and Engineering* 256, 213–225.
- Shutov, A.V., Ihlemann, J., 2014. Analysis of some basic approaches to finite strain elastoplasticity in view of reference change. *International Journal of Plasticity* 63, 183–197.
- Silbermann, C.B., Shutov, A.V., Ihlemann, J., 2014. On operator split technique for the time integration within finite strain viscoplasticity in explicit FEM. *Proceedings in Applied Mathematics and Mechanics* 14(1), 355–356.
- Simo, J.C., Ortiz, M., 1985. A unified approach to finite deformation elastoplastic analysis based on the use of hyperelastic constitutive equations. *Computer Methods in Applied Mechanics and Engineering* 49(2), 221–245.
- Simo, J.C., Ju, J.W., 1989. On continuum damage-elastoplasticity at finite strains. A computational framework. *Computational Mechanics* 5, 375–400.
- Simo, J.C., Miehe, C., 1992. Associative coupled thermoplasticity at finite strains: formulation, numerical analysis and implementation, *Computer Methods in Applied Mechanics and Engineering* 98, 41–104.
- Soyarslan, C., Tekkaya, A.E., 2010. Finite deformation plasticity coupled with isotropic damage: Formulation in principal axes and applications. *Finite Elements in Analysis and Design* 46, 668–683.

- Steinmann, P., Miehe, C., Stein, E., 1994. Comparison of different finite deformation inelastic damage models within multiplicative elastoplasticity for ductile materials. *Computational Mechanics* 13, 458–474.
- Su, J.F., Nie, X.Y., Stoilov, V., 2010. Characterization of fracture and debonding of Si particles in AlSi alloys. *Materials Science and Engineering A* 527, 7168–7175.
- Tsakmakis, Ch., Willuweit, A., 2004. A comparative study of kinematic hardening rules at finite deformations. *Int. J. Non-Linear Mech.* 39(2), 539–554.
- Tutyshkin, N., Müller, W. H., Wille, R., Zapara, M., 2014. Strain-induced damage of metals under large plastic deformation: Theoretical framework and experiments. *International Journal of Plasticity* 59, 133–151.
- Tvergaard V., 1989. Material failure by void growth to coalescence. *Advances in Applied Mechanics* 27(C), 83–151.
- Voyiadjis, G.Z., Park, T., 1999. The kinematics of damage for finite-strain elasto-plastic solids. *International Journal of Engineering Science* 37, 803–830.
- Voyiadjis, G.Z., Yousef, M.A., Kattan, P.I., 2012. New tensors for anisotropic damage in continuum damage mechanics. *Journal of Engineering Materials and Technology* 134(2), 021015.
- Wagner, S., Podlesak, H., Siebeck, S., Nestler, D., Wagner, M.F.-X., Wielage, B., Hockauf, M., 2010. Effect of ECAP and heat treatment on microstructure and mechanical properties of a SiC reinforced Al–Cu alloy. *Materials Science and Engineering Technology* 143(9), 704–710.
- Wagoner, R.H., Lim, H., Lee, M.-G., 2013. Advanced Issues in springback. *International Journal of Plasticity* 45, 3–20.
- Xiao, H., Bruhns, O. T., Meyers, A., 2006. Elastoplasticity beyond small deformations. *Acta Mechanica* 182, 31–111.
- Xue, L., 2007. Ductile Fracture Modeling – Theory, Experimental Investigation and Numerical Verification. PhD thesis, Massachusetts Institute of Technology.
- Zapara, M. A., Tutyshkin, N. D., Müller, W. H., Wille, R., 2010. Experimental study and modeling of damage of Al alloys using tensor theory. *Continuum Mech. Thermodyn.* 22, 99–120.
- Zapara, M., Tutyshkin, N., Müller, W.H., Wille, R., 2012. Constitutive equations of a tensorial model for ductile damage of metals. *Continuum Mech. Thermodyn.* 24, 697–717.
- Zhu, Y., Kang, G., Kan, Q., Yu, C., Ding, J., 2013. An extended cyclic plasticity model at finite deformations describing the Bauschinger effect and ratchetting behaviour, 13th International Conference on Fracture, June 16–21, 2013, Beijing, China.